JOURNAL OF PETROLOGY

Journal of Petrology, 2020, 1–25
doi: 10.1093/petrology/egaa099
Advance Access Publication Date: 24 October 2020
Original Manuscript

OXFORD

High-Mg# Adakitic Rocks Formed by Lower-crustal Magma Differentiation: Mineralogical and Geochemical Evidence from Garnet-bearing Diorite Porphyries in Central Tibet

Jun Wang[1], Wei Dan[1,2]*, Qiang Wang[1,2,3]* and Gong-Jian Tang [1,2]

[1]State Key Laboratory of Isotope Geochemistry, Guangzhou Institute of Geochemistry, Chinese Academy of Sciences, Guangzhou, 510640, China; [2]CAS Center for Excellence in Deep Earth Science, Guangzhou, 510640, China; [3]College of Earth and Planetary Sciences, University of Chinese Academy of Sciences, Beijing, 100049, China

*Corresponding Authors: Wei Dan, E-mail: danwei@gig.ac.cn; Qiang Wang, E-mail: wqiang@gig.ac.cn

Received 6 March 2020; Accepted 12 October 2020

ABSTRACT

Modern arc adakites with high Mg# values (molar 100 × Mg/(Mg + Fe) ratio) are generally considered products of interaction between melts derived from subducted oceanic crust and/or eroded forearc crust and peridotite in the mantle wedge. An alternative model, in which high-Mg# adakitic rocks are produced by garnet fractionation of mantle-derived magmas, has been proposed based on whole-rock geochemical variations; however, magmatic garnet has not been found in high-Mg# adakitic rocks, and little is known about the physical conditions required for this magmatic differentiation. Here we report geochronological, mineralogical and geochemical data for Late Triassic garnet-bearing high-Mg# (Mg# = 45–56) adakitic diorite porphyries and garnet-free non-adakitic diorite porphyries with Mg# > 62 from central Tibet. Consistent compositional correlation between Ca-rich garnet crystals, their host rocks and zircon autocrysts suggests that the garnet crystals grew in their host magmas. Amphibole, garnet, zircon and the host rocks display increasing Dy/Yb ratios with increasing magma differentiation. Pristine magmas in equilibrium with amphibole that crystallized prior to garnet are not adakitic. The garnet-bearing high-Mg# adakitic rocks were probably generated by the fractionation of pyroxene, amphibole and garnet at ~1 GPa from a primitive andesitic parent that was geochemically similar to the garnet-free diorite porphyries. The primitive andesitic magmas with enriched isotope compositions ($[^{87}Sr/^{86}Sr]_i > 0{\cdot}709$, $\varepsilon Nd[t] < -3{\cdot}4$) may be derived from shallow melting of subduction-enriched lithospheric mantle in a post-collisional, extensional setting resulting from oceanic slab breakoff. The most likely scenario for garnet crystallization is that mantle-derived hydrous (H_2O >5 wt %) magmas stalled, cooled isobarically and differentiated at the base of the crust. This study provides direct mineralogical evidence for the generation of high-Mg# adakitic rocks by crystal fractionation involving garnet, rather than by interaction between crust-derived melt and the mantle, although the latter is potentially a frequent occurrence in the mantle wedge.

Key words: High-Mg# adakites; slab melting; garnet; amphibole; magma differentiation

INTRODUCTION

The term 'adakite' was originally defined by Defant and Drummond (1990) as intermediate to felsic (≥56 wt % SiO_2) arc magmatic rocks produced by the melting of young (≤25 Ma) subducted oceanic crust. Adakites are characterized by Al_2O_3 and MgO contents of ≥15 wt % and usually <3 wt % (rarely >6 wt %), respectively; low Y (≤18 ppm) and Yb (≤1·9 ppm) contents; and high Sr

contents (≥400 ppm) relative to normal island-arc andesites, dacites and rhyolites (Defant & Drummond, 1990). However, many later studies have found that most adakites, including those first documented on Adak Island (Kay, 1978), have higher MgO, Cr and Ni contents, and Mg# values (molar 100 × Mg/(Mg + Fe) ratio) at a given SiO_2 content than experimentally produced melts of eclogites and garnet amphibolites (equivalent to subducted basalts). This disparity has been attributed to interaction between slab-derived melts and peridotite in the mantle wedge (e.g. Kay, 1978; Kay *et al.*, 1993; Sen & Dunn, 1994; Yogodzinski *et al.*, 1995; Rapp *et al.*, 1999; Martin *et al.*, 2005). The forearc crust may be dragged into the subduction channel due to subduction erosion, and it can be incorporated into the source of arc adakites (Goss *et al.*, 2013; Kay *et al.*, 2019). Understanding the interaction between the subducted crust-derived melts and mantle could improve our understanding of the generation of continental crust with a high-Mg# andesitic signature (Kelemen, 1995), subcratonic lithospheric mantle with a high proportion of orthopyroxene (Rapp *et al.*, 2010) and porphyry-type deposits, which contain about 75% of the world's copper (Mungall, 2002).

It has also been proposed that rocks with high-Mg# adakitic signatures can be produced by garnet (± amphibole) fractionation from hydrous mantle-derived magmas, or by mixing of mafic with felsic magmas formed by lower crustal melting in the amphibole and garnet stability fields (e.g. Castillo *et al.*, 1999; Macpherson *et al.*, 2006; Streck et al., 2007; Zellmer *et al.*, 2012). Garnet fractionation in the deep crust has been indirectly inferred from whole-rock geochemical variations, such as the relationship between Dy/Yb ratios and SiO_2 contents (e.g. Macpherson *et al.*, 2006; Shibata *et al.*, 2015). To our knowledge, however, garnet has not been identified as a magmatic phase in high-Mg# adakitic rocks, hence little is known about the physical conditions of this fractionation. Instead, garnet phenocrysts have been found in some intermediate–felsic rocks with low Sr contents (<400 ppm) and Sr/Y ratios (<40) (e.g. Day *et al.*, 1992; Harangi *et al.*, 2001; Yuan *et al.*, 2009; Shuto *et al.*, 2013; Luo *et al.*, 2018), implying plagioclase fractionation but no significant garnet fractionation during the rapid ascent of the host magmas; therefore, the garnet-fractionation model for the generation of high-Mg# adakitic rocks needs further verification.

Garnet and amphibole that crystallize at different stages may have different textural and geochemical signatures, and compositional variations can be used to elucidate the evolution of melts in equilibrium with their crystals (e.g. Bach *et al.*, 2012; Ribeiro *et al.*, 2016; Tang *et al.*, 2017; Zhou *et al.*, 2020). Their compositions in particular contain information about magma crystallization depths (e.g. Green, 1977; Harangi *et al.*, 2001; Prouteau & Scaillet, 2003; Ridolfi & Renzulli, 2012), and can provide evidence of parental magma compositions that whole-rock compositions cannot, especially when late-stage differentiation has obscured primary-melt features.

Here we present a detailed geochronological, mineralogical and geochemical study of garnet-bearing Late Triassic high-Mg# adakitic diorite porphyries from central Tibet. These rocks were most likely generated by the fractionation of pyroxene, amphibole and garnet from a primitive andesitic parent at lower crustal pressures (~1 GPa). This study provides direct mineralogical evidence of the importance of lower-crustal garnet fractionation in the generation of high-Mg# adakitic rocks, which does not require interaction between crust-derived melts and the mantle, although this interaction is potentially a frequent occurrence in the mantle wedge.

GEOLOGICAL SETTING AND PETROGRAPHY

The Tibetan Plateau in east-central Asia (Fig. 1a) was developed by the successive closure of the multiple Tethyan oceans between the Laurasia and various Gondwana-derived terranes since the Paleozoic (Yin and Harrison, 2000). The Qiangtang Terrane in the central Tibetan Plateau is separated from the Hoh Xil–Songpan–Garzê Terrane by the Jinsha suture to the north and from the Lhasa Terrane by the Bangong–Nujiang suture to the south (Fig. 1a). The Longmu Co–Shuanghu suture that separates the Northern and Southern Qiangtang terranes has been interpreted as being an *in situ* Paleo-Tethyan suture zone. It includes Triassic blueschists and eclogites and Carboniferous and Permian ophiolites (Zhai *et al.*, 2011; Zhang *et al.*, 2016; Dan *et al.*, 2018a). Zircon U–Pb ages (237–230 Ma) and mineral Lu–Hf isochron ages (244–233 Ma) of the Qiangtang eclogites are thought to represent the age of peak eclogite-facies metamorphism (Pullen *et al.*, 2008; Zhai *et al.*, 2011). Dan *et al.* (2018a) obtained zircon U–Pb ages of 238 ± 1 Ma for the Qiangtang eclogites, which they interpreted as being the formation age of the protoliths of the eclogites, and concluded that the 233 Ma peak-metamorphism age marks the collision between the Northern and Southern Qiangtang terranes and closure of the Paleo-Tethys Ocean. Phengite $^{40}Ar/^{39}Ar$ ages (223–214 Ma) of the eclogites and schists were interpreted as being the exhumation age of the Qiangtang eclogites (Zhai *et al.*, 2011).

Previous studies have shown that magmatism in the Northern Qiangtang terrane ranged from Late Devonian to early Carboniferous and from middle Permian to Late Triassic in age (Fig. 1a, Zhai *et al.*, 2013; Dan *et al.*, 2018b, 2019; Wang *et al.*, 2018b and references therein), and pre-Late Triassic magmatism has been attributed to northward Paleo-Tethys subduction. Zircon U–Pb age data for Late Triassic magmatic rocks and $^{40}Ar/^{39}Ar$ age data from high-pressure metamorphic rocks indicate that peak metamorphic rock exhumation and peak magmatism around the Longmu Co–Shuanghu suture was coeval at 225–205 Ma (Fig. 1a, Wu *et al.*, 2016).

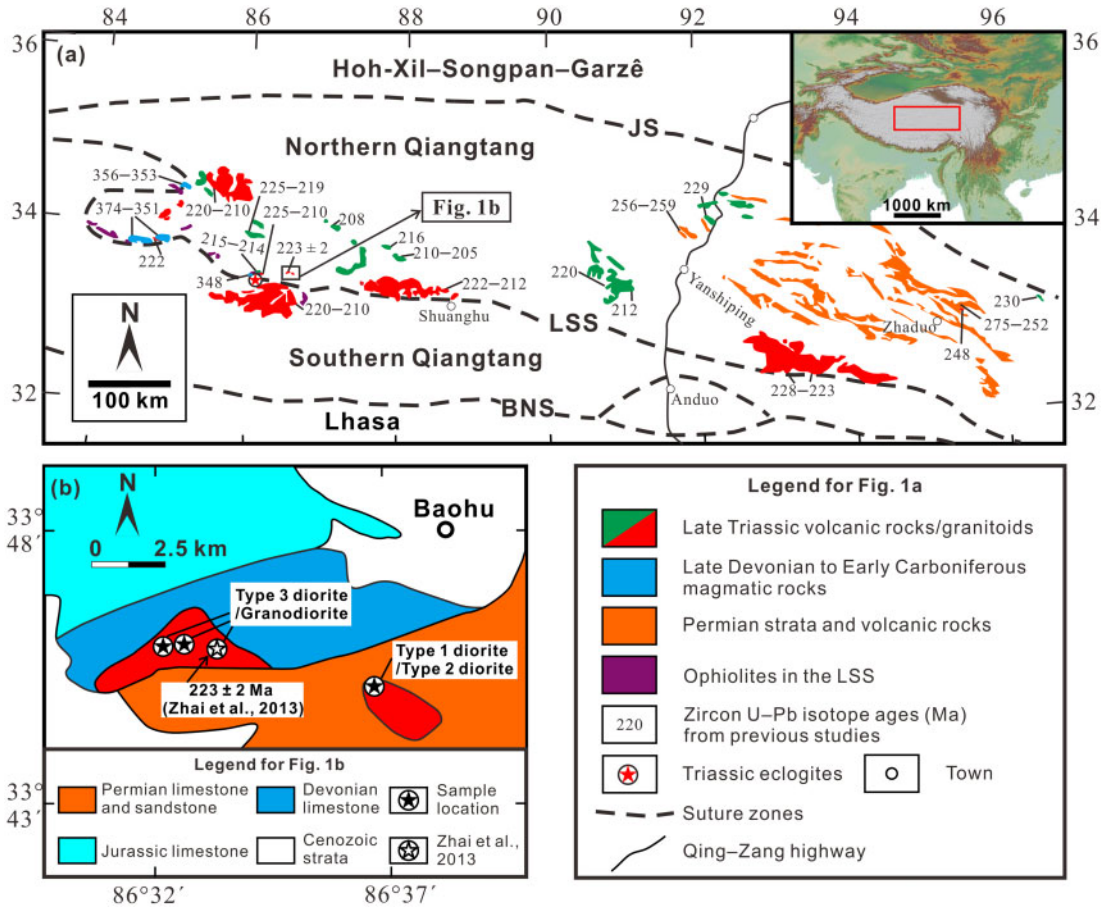

Fig. 1. (a) Simplified geological map of the central Tibetan Plateau, showing the major terranes and the distribution of Late Devonian to Late Triassic igneous rocks in the Northern Qiangtang Terrane. The map and ages are from Wang *et al.* (2018b) and references therein. (b) Geological map showing the two plutons in the Baohu area of the Northern Qiangtang Terrane (modified from Zhai *et al.*, 2013). LSS, Longmu Co–Shuanghu suture; JS, Jinshajiang suture; BNS, Bangong–Nujiang suture.

Two plutons were discovered in the Baohu area, approximately 50 km northeast of the Pianshishan eclogites (red star in Fig. 1a), intruding Devonian and Permian limestones and sandstones (Fig. 1b). We collected 16 diorite samples from these plutons, in which the proportions of amphibole and quartz are significantly different although all samples are named diorite porphyry (Table 1). The diorites from the eastern pluton have porphyritic textures, and can be further divided into two types based on their phenocrysts (Fig. 1b, Table 1). The primary phenocryst phase within Type 1 diorite porphyries is amphibole (1·0–2·5 mm; ~25 vol.%), which is dispersed in a fine-grained matrix (0·1–0·4 mm) comprising amphibole, plagioclase and minor oxides (Fig. 2a). Amphibole phenocrysts are commonly unzoned, but some have wide, dark cores with narrow, light-coloured rims in back-scattered-electron (BSE) images (the colours are reversed in photomicrographs taken under plane-polarized light; Fig. 2c). The colour of the rim is similar to that of adjacent amphibole microcrysts within the matrix. A few amphibole phenocrysts have small pyroxene inclusions that have been altered to form actinolite. The phenocrysts (~30 vol.%) in Type 2 diorite porphyries comprise plagioclase and minor amphibole and garnet (<5 vol.%; 2·5–5·0 mm; Fig. 2b). Garnet phenocrysts are slightly rounded and have cracks and resorbed, irregular margins (Fig. 2d). Inclusions in garnet are rare and comprise mainly plagioclase, apatite, and oxides. The Type 2 diorites are more altered than the Type 1 diorites. Amphibole is generally replaced by chlorite (Fig. 2b), and plagioclase has undergone significant sericitization and/or saussuritization (Fig. 2d); therefore, we did not obtain compositional data for the plagioclase and amphibole in Type 2 diorite.

Zhai *et al.* (2013) have previously reported zircon U–Pb ages and whole-rock geochemical compositions of the western pluton (Fig. 1b), which has adakitic signatures. The samples they collected include diorite porphyries and granodiorite porphyries. Our new diorite samples (Type 3 diorite) also have porphyritic textures with 20–40 vol.% phenocrysts comprising plagioclase and occasional amphibole and quartz in a groundmass of feldspar, amphibole, and quartz microlites (Fig. 2e). In addition to the mineral assemblage reported by Zhai *et al.* (2013), brown garnet crystals (0·5–1·5 mm) are observed in the hand specimen, and occur either as small inclusions within large plagioclase phenocrysts

Table 1: The localities and main characteristics of the Baohu diorite porphyries.

Samples	Longitude	Latitude	SiO_2 (wt%)	Mg#	Sr/Y	Age (Ma)	Phenocrysts	Groundmass
Type 1 diorite porphyry (the eastern pluton)								
GZ114-7	86°36′47″E	33°45′23″N	55·6	65	21		Amp (~25%).	Amp, Pl, Oxides.
GZ114-8	86°36′47″E	33°45′23″N	56·5	64	23	219		
GZ114-9	86°36′47″E	33°45′23″N	58·0	62	27			
GZ114-10	86°36′47″E	33°45′23″N	56·6	64	15			
GZ114-11	86°36′47″E	33°45′23″N	57·3	65	23			
Type 2 diorite porphyry (the eastern pluton)								
GZ114-1	86°36′47″E	33°45′23″N	60·5	50	43		Pl (15–25%), Amp	Pl, Amp, Qtz,
GZ114-2	86°36′47″E	33°45′23″N	60·6	52	42	220	(~5%), Grt	Oxides.
GZ114-3	86°36′47″E	33°45′23″N	60·2	54	33		(<5%).	
GZ114-5	86°36′47″E	33°45′23″N	60·8	53	36			
GZ114-6	86°36′47″E	33°45′23″N	60·3	56	35			
Type 3 diorite porphyry (the western pluton)								
GZ111-1	86°32′10″E	33°45′47″N	62·0	45	107		Pl (20–30%), Amp	Pl, Amp, Qtz,
GZ111-2	86°32′10″E	33°45′47″N	61·8	46	104		(5–10%),Qtz	Oxides.
GZ111-3	86°32′10″E	33°45′47″N	62·1	47	99	222	(~5%), Grt	
GZ111-4	86°32′10″E	33°45′47″N	62·0	49	101		(<5%).	
GZ112-1	86°32′25″E	33°45′49″N	61·2	49	55			
GZ112-2	86°32′25″E	33°45′49″N	61·5	50	53			

Mg# = molar 100 × Mg/(Mg + Fe_{totoal}); Amp, amphibole; Pl, plagioclase; Grt, garnet; Qtz, quartz.

(Fig. 2e–g), or as small phenocrysts (Fig. 2h) within the matrix. Garnet does not exceed ~5 vol.% and always has embayed, irregular margins. Garnet phenocrysts in contact with the groundmass are characterized by reaction coronas of fine-grained, interlocking plagioclase + amphibole (with chlorite alteration) ± oxides (Fig. 2h). A fresh amphibole macrocryst (~18 mm) with embayed edges and resorption channels was found in a Type 3 diorite sample (GZ111-3; Fig. 2e–f). Relatively small amphibole phenocrysts (1·0–4·0 mm) are present as either euhedral crystals with straight edges (Fig. 2i) or anhedral crystals with embayed edges (Fig. 2j). Most amphibole phenocrysts are replaced by chlorite or actinolite along their cleavage planes, and we were able to acquire only a little amphibole compositional data. Small, euhedral amphibole (0·1–0·3 mm) inclusions occur in some large plagioclase phenocrysts (Fig. 2k).

ANALYTICAL METHODS

Whole-rock geochemistry

The samples for whole-rock elemental and isotopic analyses were crushed to coarse chips and fresh pieces were handpicked. To avoid surface contamination and remove calcite-filled amygdales, the rock chips were cleaned twice with 2% HCl, rinsed twice with Milli-Q water, and then powdered to ~200 mesh with an agate mortar and pestle. Major-element oxides were analysed in fused glass beads using a Rigaku RIX 2000 X-ray fluorescence spectrometer at the State Key Laboratory of Isotope Geochemistry (SKLaBIG), Guangzhou Institute of Geochemistry, Chinese Academy of Sciences (CAS), Guangzhou, China, following the procedures of Li *et al.* (2006). Analytical uncertainties were 1%–5%. Trace-element compositions were determined using a Perkin-Elmer ELAN 6000 inductively coupled plasma–mass spectrometer (ICP–MS) at the SKLaBIG, following procedures described by Li *et al.* (2006). About 40 mg of each powdered sample was dissolved in a high-pressure Teflon bomb for 2 days at 190 °C using a mixture of HF + HNO_3 + $HClO_4$ (1:1:0·2). Analytical precision was 2–5%.

Whole-rock Sr–Nd isotopic ratios were determined using a Neptune multicollector (MC) ICP–MS at the SKLaBIG, using analytical procedures described by Li *et al.* (2006). All isotopic ratios were corrected for fractionation using a $^{86}Sr/^{88}Sr$ ratio of 0·1194 and a $^{146}Nd/^{144}Nd$ ratio of 0·7219. Reported $^{87}Sr/^{86}Sr$ and $^{143}Nd/^{144}Nd$ ratios were further adjusted relative to the NBS SRM 987 ($^{87}Sr/^{86}Sr$ = 0·71025) and the Shin Etsu JNdi-1 standard ($^{143}Nd/^{144}Nd$ = 0·512115), respectively. The basaltic standard BHVO-2 was used to monitor ion-exchange chromatographic purification, and yielded a $^{87}Sr/^{86}Sr$ ratio of 0·703483 ± 0·000014 (2 standard error, SE) and a $^{143}Nd/^{144}Nd$ ratio of 0·512978 ± 0·000008 (2SE), consistent with the certified values of $^{87}Sr/^{86}Sr$ = 0·703481 ± 0·000020 and $^{143}Nd/^{144}Nd$ = 0·512983 ± 0.000010, respectively (Weis *et al.*, 2005). Major-element, trace-element and Sr–Nd isotope data are listed in Table 2.

Zircon U–Pb, Hf and O isotopic and trace-element compositions

Prior to isotopic analyses, cathodoluminescence (CL) images of zircons were acquired using a JEOL JXA-8100 electron microprobe at the SKLaBIG. Zircon oxygen isotopic compositions were determined prior to U–Pb analysis using a CAMECA IMS 1280-HR secondary-ion mass spectrometer (SIMS) at the SKLaBIG, and applying the analytical procedure described by Li *et al.* (2010). The data were corrected for instrumental mass fractionation using the Penglai zircon standard ($\delta^{18}O_{VSMOW}$ = 5·3‰, Li *et al.*, 2010), and the internal precision of a single $^{18}O/^{16}O$ analysis was better than 0·38‰ (2SE). External precision, measured by the reproducibility of repeated analyses of the

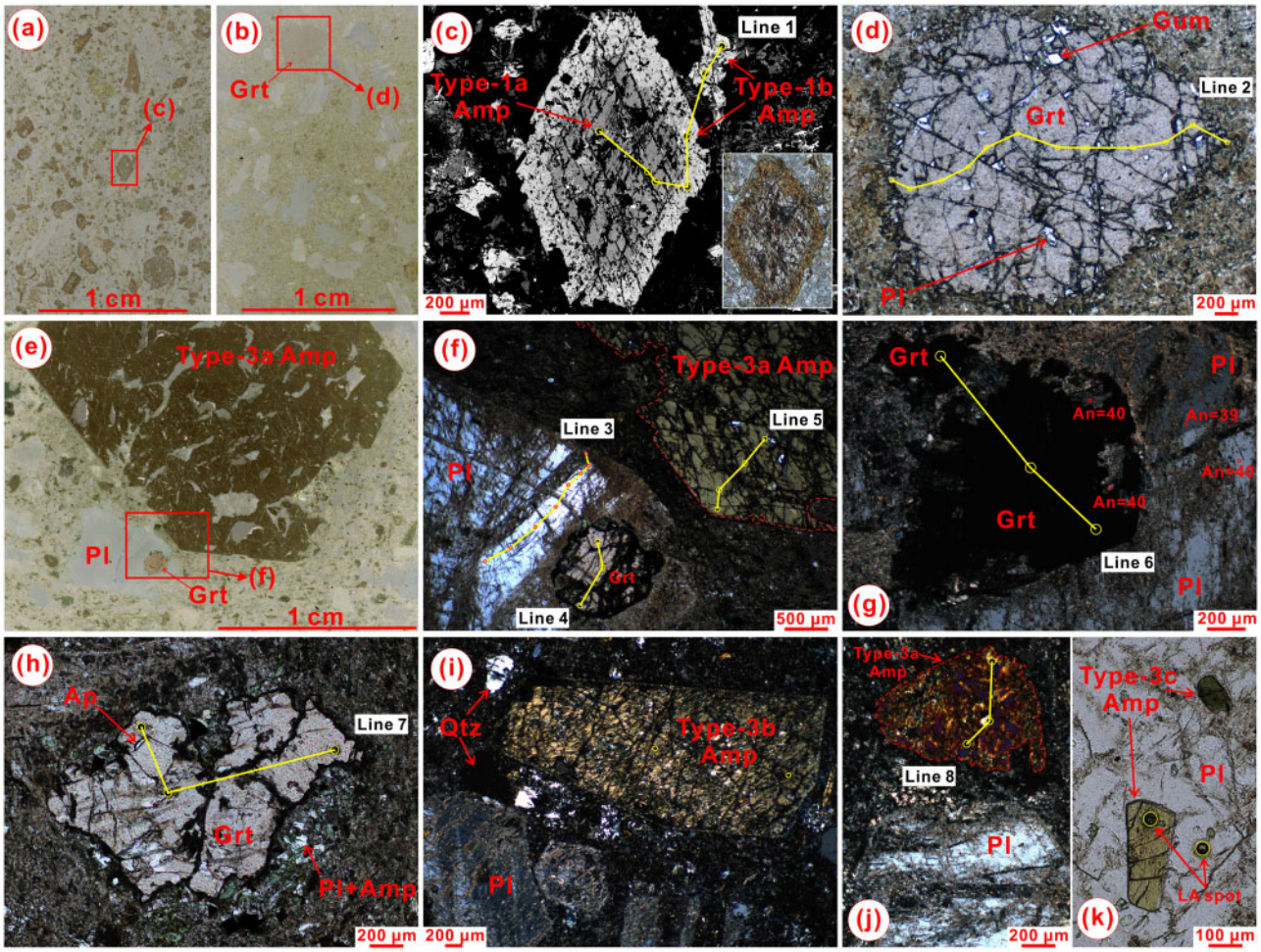

Fig. 2. (a) Photograph of a thin section of Type 1 diorite (sample GZ114-7). The red rectangle indicates the area shown in Fig. 2c. (b) Photograph of a thin section of Type 2 diorite (sample GZ114-5). The red rectangle indicates the area shown in Fig. 2d. (c) BSE image of a zoned amphibole phenocryst. The inset shows a photomicrograph of the same area under plane-polarized light (PPL). (d) Photomicrograph of a garnet phenocryst with plagioclase inclusions and cracks filled with epoxy (PPL). (e) Photograph of a thin section of Type 3 diorite (sample GZ111-3), showing an amphibole macrocryst with resorption channels. The red rectangle indicates the area shown in Fig. 2f. (f) Photomicrograph of a plagioclase phenocryst with a garnet inclusion and an amphibole macrocryst with resorbed boundaries (PPL). (g) Photomicrograph of an anhedral garnet crystal from sample GZ111-3, with small plagioclase inclusions in its rim, included in a large plagioclase phenocryst under crossed polarized light (XPL). Note that the small plagioclase inclusions and adjacent host plagioclase have the same extinction position. (h) Photomicrograph of a garnet phenocryst from a Type 3 diorite (sample GZ111-1) with a reaction corona made of fine-grained, interlocking plagioclase + amphibole + oxides (PPL). (i) Photomicrograph of a euhedral amphibole phenocryst with straight edges (sample GZ111-3; XPL). (j) Photomicrograph of an anhedral amphibole phenocryst with embayed edges (sample GZ111-3; XPL). (k) Photomicrograph of small, euhedral amphibole inclusions in a large plagioclase phenocryst (sample GZ111-1; PPL). Yellow and red circles show the locations of the laser-ablation and electron-microprobe analyses, respectively. The compositional profiles indicated by the yellow lines are shown in Fig. 8. Amp, amphibole; Pl, plagioclase; Grt, garnet; Qtz, quartz.

Penglai standard, was 0·48‰ (2SD; n = 19). Analyses of the Qinghu zircon standard yielded a weighted-mean $\delta^{18}O$ value of 5·7‰ ± 0·5‰ (2SD; n = 7), consistent with the certified value of 5·4‰ ± 0·2‰ (2SD, Li *et al.*, 2013). Zircon oxygen isotopic data are listed in Supplementary Data Table S1.

Zircon U–Pb isotopic and trace-element compositions were synchronously determined using an Agilent 7500a quadruple ICP–MS attached to a GeoLas-193 ArF excimer laser-ablation (LA) system at the SKLaBIG and at the Institute of Geology and Geophysics, CAS, Beijing, China. Operating conditions of the LA–ICP–MS and data reduction were as described by Xie *et al.* (2008). $^{207}Pb/^{235}U$ and $^{206}Pb/^{238}U$ ratios were calculated using the ICPMSDataCal software (Liu *et al.*, 2010) with zircon standard 91500 used as an external standard. Trace-element concentrations were calculated using Si as the internal standard and NIST 610 as the reference standard. The precision and accuracy of the zircon 91500 analyses were 2–15% for most elements (excluding La). Weighted-mean U–Pb ages and concordia plots were generated using Isoplot/Ex v. 3.0 (Ludwig, 2003). Analyses of the GJ-1 and Plešovice zircon standards yielded weighted-mean $^{206}Pb/^{238}U$ ages of 611 ± 6 Ma

Table 2 Major (wt %) and trace (ppm) element and Sr–Nd isotope data for the Baohu diorite porphyries.

Sample	GZ111-1	GZ111-2	GZ111-3	GZ111-4	GZ112-1	GZ112-2	GZ114-1	GZ114-2
Rock type	Type 3	Type 3	Type 3	Type 3	Type 3	Type 3	Type 2	Type 2
SiO_2	62·00	61·85	62·06	61·96	61·22	61·45	60·54	60·58
TiO_2	0·45	0·43	0·47	0·44	0·47	0·47	0·47	0·46
Al_2O_3	17·81	17·88	17·74	17·75	17·66	17·67	17·55	17·48
Fe_2O_3	4·73	4·75	4·57	4·56	5·10	5·15	5·63	5·65
MnO	0·10	0·10	0·08	0·08	0·10	0·10	0·11	0·12
MgO	1·95	2·05	2·03	2·21	2·44	2·55	2·80	3·13
CaO	4·12	4·02	4·15	3·90	3·65	3·45	1·80	1·56
Na_2O	5·10	5·24	4·84	4·95	5·06	4·74	7·36	6·89
K_2O	1·38	1·15	1·53	1·56	1·49	1·72	0·44	0·86
P_2O_5	0·09	0·10	0·10	0·10	0·09	0·09	0·09	0·09
LOI	1·91	2·09	1·95	2·17	2·37	2·27	2·84	2·82
Total	99·65	99·66	99·52	99·67	99·66	99·67	99·64	99·64
Sc	8·50	8·70	8·23	8·40	9·91	10·5	11·3	12·1
V	50·1	51·8	50·0	48·8	56·4	59·5	69·6	71·8
Cr	189	187	13·1	13·0	19·8	20·0	138	173
Ni	17·0	18·4	7·22	7·17	7·87	8·30	23·2	29·3
Ga	19·6	19·4	19·6	19·3	18·5	19·1	18·3	18·5
Rb	49·2	42·5	55·0	57·1	52·0	65·9	14·3	26·5
Sr	939	984	887	900	648	633	387	377
Y	8·81	9·49	9·00	8·89	11·7	12·0	8·93	9·09
Zr	95·8	110	91·9	94·9	105	87·7	94·0	87·7
Nb	2·86	2·96	2·80	2·72	2·54	2·58	2·59	2·55
Cs	2·81	2·92	3·19	3·20	2·56	3·38	0·36	0·80
Ba	359	287	364	354	386	400	138	361
La	9·70	11·5	14·5	9·39	12·4	12·9	10·8	9·93
Ce	19·8	23·9	29·8	19·1	24·6	25·6	21·9	20·1
Pr	2·58	3·13	3·71	2·46	3·05	3·15	2·70	2·48
Nd	10·7	12·8	14·9	10·4	12·3	12·4	10·6	9·95
Sm	2·40	2·71	2·96	2·31	2·56	2·58	2·18	2·04
Eu	0·78	0·83	0·84	0·77	0·81	0·82	0·66	0·64
Gd	2·29	2·47	2·58	2·26	2·42	2·51	2·05	1·96
Tb	0·33	0·38	0·35	0·33	0·38	0·39	0·30	0·30
Dy	1·76	2·01	1·83	1·76	2·17	2·25	1·73	1·70
Ho	0·34	0·37	0·34	0·34	0·46	0·47	0·35	0·37
Er	0·88	0·94	0·89	0·88	1·27	1·30	1·01	1·04
Tm	0·13	0·14	0·13	0·13	0·19	0·19	0·15	0·16
Yb	0·78	0·88	0·81	0·81	1·22	1·24	0·98	1·05
Lu	0·12	0·13	0·13	0·13	0·20	0·20	0·16	0·17
Hf	2·84	3·30	2·82	2·88	3·08	2·63	2·75	2·64
Ta	0·26	0·26	0·27	0·26	0·25	0·25	0·24	0·24
Pb	11·2	10·3	12·5	14·2	21·6	20·4	9·05	7·20
Th	3·22	4·01	4·97	3·11	4·68	4·61	4·47	4·43
U	1·35	1·73	1·55	1·32	1·22	1·37	1·26	1·36
$(^{143}Nd/^{144}Nd)_S$	0·512456		0·512417					0·512362
1SE	0·000005		0·000004					0·000005
εNd(t)	−1·86		−2·15					−3·36
$(^{87}Sr/^{86}Sr)_S$	0·708521		0·708619					0·709914
1SE	0·000008		0·000007					0·000008
$(^{87}Sr/^{86}Sr)_i$	0·708042		0·708053					0·709278

Sample	GZ114-3	GZ114-5	GZ114-6	GZ114-7	GZ114-8	GZ114-9	GZ114-10	GZ114-11
Rock type	Type 2	Type 2	Type 2	Type 1	Type 1	Type 1	Type 1	Type 1
SiO_2	60·20	60·78	60·34	55·58	56·48	58·03	56·59	57·34
TiO_2	0·48	0·49	0·47	0·56	0·54	0·52	0·57	0·55
Al_2O_3	17·57	17·76	17·61	16·51	16·37	16·50	16·35	16·30
Fe_2O_3	5·63	5·50	5·47	6·59	6·45	5·94	6·42	6·37
MnO	0·12	0·11	0·10	0·14	0·13	0·12	0·13	0·12
MgO	3·30	3·15	3·47	6·23	5·79	4·94	5·72	5·93
CaO	1·57	1·44	1·92	4·52	4·69	4·41	4·79	4·46
Na_2O	6·90	7·04	6·26	4·86	4·89	5·46	5·72	4·79
K_2O	0·82	0·89	1·16	1·45	1·52	1·31	0·96	1·48
P_2O_5	0·09	0·09	0·09	0·07	0·07	0·07	0·07	0·08
LOI	2·98	2·40	2·79	3·16	2·73	2·34	2·34	2·27
Total	99·67	99·66	99·68	99·67	99·67	99·65	99·66	99·67
Sc	12·7	12·1	13·3	21·5	20·6	17·7	19·8	20·0
V	75·7	71·8	75·5	126	121	107	119	118
Cr	193	139	55	303	332	183	338	215
Ni	30·8	22·7	19·5	80·7	80·4	60·1	79·2	73·7

(continued)

Table 2 Continued

Sample	GZ114-3	GZ114-5	GZ114-6	GZ114-7	GZ114-8	GZ114-9	GZ114-10	GZ114-11
Rock type	Type 2	Type 2	Type 2	Type 1	Type 1	Type 1	Type 1	Type 1
Ga	19·0	18·2	19·7	17·9	17·5	17·5	17·4	17·4
Rb	24·5	26·0	39·2	57·6	56·1	39·0	28·0	50·0
Sr	324	373	397	287	307	305	207	313
Y	9·69	10·5	11·4	13·8	13·4	11·5	13·4	13·5
Zr	86·0	98·9	98·6	84·6	84·7	93·8	89·7	87·1
Nb	2·57	2·65	2·69	2·08	2·12	2·36	2·17	2·24
Cs	0·91	2·67	5·16	31·8	22·2	1·32	15·7	3·43
Ba	305	366	514	580	544	496	222	412
La	11·7	12·3	12·5	9·70	9·88	10·8	10·3	10·7
Ce	23·0	24·5	25·0	19·7	19·9	21·4	20·6	21·5
Pr	2·84	3·01	3·09	2·54	2·53	2·60	2·60	2·69
Nd	11·3	11·9	12·4	10·5	10·5	10·5	10·7	10·9
Sm	2·28	2·44	2·51	2·44	2·35	2·26	2·38	2·43
Eu	0·72	0·75	0·78	0·74	0·73	0·72	0·77	0·74
Gd	2·17	2·35	2·49	2·54	2·48	2·31	2·47	2·52
Tb	0·33	0·36	0·38	0·43	0·41	0·36	0·41	0·41
Dy	1·86	2·06	2·14	2·56	2·44	2·17	2·45	2·46
Ho	0·39	0·42	0·45	0·55	0·52	0·45	0·53	0·52
Er	1·06	1·14	1·21	1·55	1·46	1·27	1·46	1·47
Tm	0·16	0·17	0·18	0·23	0·22	0·19	0·22	0·22
Yb	1·07	1·08	1·14	1·45	1·41	1·23	1·39	1·40
Lu	0·17	0·17	0·18	0·24	0·23	0·20	0·23	0·23
Hf	2·67	2·87	2·86	2·43	2·42	2·59	2·54	2·56
Ta	0·23	0·24	0·26	0·19	0·19	0·23	0·19	0·22
Pb	8·04	13·5	11·2	6·36	8·01	9·42	8·71	13·3
Th	4·50	4·54	4·61	3·73	3·68	4·03	3·69	4·12
U	1·45	1·30	1·45	1·17	1·22	1·05	1·20	1·30
$(^{143}Nd/^{144}Nd)_S$					0·512365		0·512377	0·512374
1SE					0·000004		0·000006	0·000005
εNd(t)					−3·64		−3·38	−3·46
$(^{87}Sr/^{86}Sr)_S$					0·71075		0·710368	0·710581
1SE					0·000008		0·00001	0·000009
$(^{87}Sr/^{86}Sr)_i$					0·709094		0·709145	0·709136

(2SD; n = 7) and 336 ± 4 Ma (2SD; n = 6), respectively, consistent with certified values (Sláma *et al.*, 2008 and references therein). LA–ICP–MS zircon U–Pb isotopic and trace-element data are presented in Supplementary Data Table S2 and Table S3, respectively.

Zircon Hf isotopic analyses were undertaken on the same zircons using a Neptune Plus MC–ICP–MS attached to a 193 nm (ArF) Resonetics RESOlution M-50 LA System at the SKLaBIG, with a beam diameter of 45 μm Analytical procedures have been described by Zhang *et al.* (2015). Analyses of the Plešovice zircon standard yielded a weighted-mean $^{176}Hf/^{177}Hf$ ratio of 0·282488 ± 0·000011 (2SD; n = 12), consistent with the certified value (Sláma *et al.*, 2008). Zircon Hf isotopic data are given in Supplementary Data Table S1.

Mineral major- and trace-element compositions

Mineral major-element compositions were determined at the SKLaBIG using a JXA-8100 electron microprobe (EMP) with an accelerating voltage of 15 kV, a beam current of 20 nA and a beam diameter of 1–2 μm Analytical uncertainties were generally < 2%. Analytical procedures were as described by Huang *et al.* (2007) and results are given in Supplementary Data Tables S4–S6. Amphibole formulae were calculated using an excel spreadsheet from Locock (2014) that was programmed following the 2012 nomenclature recommended by the International Mineralogical Association. Garnet end-member and ferric-ion proportions were estimated using the method of Muhling & Griffin (1991).

In situ mineral trace-element compositions were determined using an Agilent 7500a ICP–MS system coupled with a 193-nm ArF excimer LA system at the SKLaBIG. A double-volume sampling cell and a squid pulse-smoothing device were used to improve data quality, with analytical techniques as described by Tu *et al.* (2011). The analyses used a spot diameter of 40 μm, and trace-element contents were based on calibrations with multiple reference materials (BCR-2G, BHVO-2G, and BIR-1G) as external standards, and Si as the internal standard. LA spots were coincident with EMP spots where possible, so that Si contents obtained using the EMP could be used for internal standardization. Repeat analyses of the GOR132-G reference glass indicated that precision and accuracy were better than 10% for the elements with concentrations >0·5 ppm (Supplementary Data Table S9). Off-line selection and integration of background and analytical signals, time-drift corrections, and quantitative calibrations were undertaken using ICPMSDataCal software (Liu *et al.*, 2010). Contamination from inclusions and fractures was monitored using several elements, with results given in Supplementary Data Tables S7 and S8.

RESULTS

Whole-rock geochemistry

As petrographic observations indicate that the Baohu porphyries have undergone varying degrees of hydrothermal alteration (Fig. 2), the potential effects of hydrothermal alteration need to be assessed before petrogenetic discussions. The chemical index of alteration (CIA = molar $100 \times Al_2O_3/[Al_2O_3 + CaO + Na_2O + K_2O]$) have been widely used to study the weathering or alteration profiles developed on lava flows and plutonic rocks (Nesbitt & Young, 1982). This is because secondary minerals (e.g. chlorite, sericite, and clay minerals) have significantly higher CIA values (75–100) than the primary silicate minerals (0–50). The Baohu porphyries have relatively low loss-on-ignition (1·9–3·2 wt %) and CIA (46–54) values, overlapping those of fresh granites and granodiorites (CIA = 45–55, Nesbitt & Young, 1982). Most element contents show no correlation with CIA values within each diorite type (Supplementary Data Fig. S2), suggesting that they were immobile during alteration. However, the Na_2O and K_2O contents of the Type 1 and 2 diorites are correlated with CIA values, indicating alteration mobilized both Na and K.

The Baohu diorite porphyries and granodiorite porphyries have a wide range of SiO_2 (57·6–71·7 wt %, on a volatile-free basis) and MgO (1·7–6·5 wt %) contents (Fig. 3). The Type 1 diorites have the lowest SiO_2 contents (57·6–59·6 wt %) but the highest MgO contents (5·1–6·5 wt %) and Mg# values (62–65) of the diorites, and fit the definition of 'primitive andesites' (54–65 wt % SiO_2; Mg# > 60; Kelemen *et al.*, 2003). In contrast, the types 2 and 3 diorites have relatively evolved compositions, with Mg# values of 45–56 and SiO_2 contents of 62·3–63·6 wt %, consistent with the definition of "high-Mg# andesites" (54–65 wt % SiO_2; Mg# = 45–60; Kelemen *et al.*, 2003).

All rock types are characterized by enrichment in large-ion lithophile elements (LILE) and depletion in high-field-strength elements (HFSE; e.g. Nb, Ta and Ti; Fig. 4b). They display fractionated rare-earth element (REE) patterns, progressive depletion in the heavy REE (HREE; Fig. 4a), and gradual increases in Sr/Y and Dy/Yb ratios (Fig. 5a, b) from Type 1 through Type 2 to Type 3 diorites and granodiorites, indicating the control of garnet fractionation on their chemical evolution. The Type 3 diorite samples have adakitic geochemical characteristics (Fig. 5a, Defant & Drummond, 1990), with high Al_2O_3 (18·1–18·3 wt %) and Sr (633–984 ppm) contents and Sr/Y ratios (53–107), low Y (8·8–12·0 ppm) and Yb (0·78–1·24 ppm) contents, no Eu anomalies and strongly positive Sr anomalies (Fig. 4). The Sr/Y ratios (33–43) of Type 2 diorites are lower than those of Type 3 diorites, but still plot into the adakite field in the Y–(Sr/Y) diagram (Fig. 5a). Type 2 diorites have lower CaO and SiO_2 and higher MgO contents than Type 3 diorites and granodiorites (Fig. 5c, d). Type 1 diorites have lower Sr contents (207–313 ppm) and Sr/Y ratios (15–26) than typical adakites (Sr > 400 ppm and Sr/Y > 22, Defant & Drummond, 1990; Fig. 5a). The types 1 and 2 diorites from the eastern pluton have similar Sr–Nd isotopic compositions, which are more enriched than those of Type 3 diorites from the western pluton (Fig. 5e).

Zircon U–Pb, Hf and O isotopic and trace-element compositions

Zircon U–Pb concordia diagrams and CL images for the Baohu diorite samples are given in Fig. 6. Zircon grains in Type 3 diorite display high-contrast, narrow oscillatory zonation; while those in the Type 1 diorite display broad zoning patterns (Fig. 6d). Zone thicknesses progressively increase from Type 3 through Type 2 to Type 1 diorite (Fig. 6d), correlated with increasing whole-rock MgO contents (Fig. 3b). The variation in zoning patterns may thus be the result of increasing diffusion coefficients with increasing temperature (Corfu *et al.*, 2003). The zircon crystals are magmatic and cognate with their host rocks. Zircon U–Pb crystallization ages (222–219 Ma) of the three diorite types are within error of each other (Fig. 6), and the weighted-mean zircon U–Pb age of the Type 3 diorites (222 ± 2 Ma; Fig. 6c) is similar to that previously reported for the same pluton (223 ± 2 Ma; Zhai *et al.*, 2013).

The REE patterns of zircon from all diorite types are characterized by positive Ce and slightly negative Eu anomalies and HREE enrichment (Fig. 6e). Zircon from the Type 3 diorites has flatter HREE patterns (Fig. 6e), higher Dy/Yb (0·43–0·85) ratios, and a wider range of Dy/Yb ratios (Fig. 6f) than those from types 1 (Dy/Yb = 0·26–0·30) and 2 (Dy/Yb = 0·13–0·22) diorites; these compositional differences are reflected in the whole-rock compositions of the host diorites (Fig. 5b). Both the zircon (Fig. 6f) and whole-rock (Fig. 5b) Dy/Yb ratios of Type 2 diorite sample GZ114-2 are slightly lower than those of Type 1 diorites, although the mean Dy/Yb ratios of types 1 and 2 diorites are indistinguishable. The compositional correlation between zircon grains and their host rocks further suggests that they are autocrysts that crystallized from host magmas, rather than xenocrysts.

Zircon O–Hf isotopes were analysed *in situ* for the three samples that were dated. Type 1 diorite zircon grains were too small for us to find large enough areas for O and Hf isotopic analyses after age analysis (Fig. 6d). Zircon grains from Type 3 diorites have mean εHf(t) values of 3·8 ± 2·3 (all errors are 2SD) and mean $\delta^{18}O$ values of 5·9 ± 1·0‰, which partially overlap with but are slightly lower than those of Type 2 diorites (εHf(t) = 5·2 ± 1·8; $\delta^{18}O$ = 6·3 ± 0·8‰; Fig. 5f).

Amphibole major- and trace-element compositions

All of the analysed amphibole belong to the calcic group; most crystals exhibit $(Na + K)^A \geq 0{\cdot}5$ apfu (atoms per formula unit) and fall in the magnesiohastingsite ($Al^{VI} < Fe^{3+}$)–pargasite ($Al^{VI} \geq Fe^{3+}$)–edenite and ferropargasite fields, but a small number are

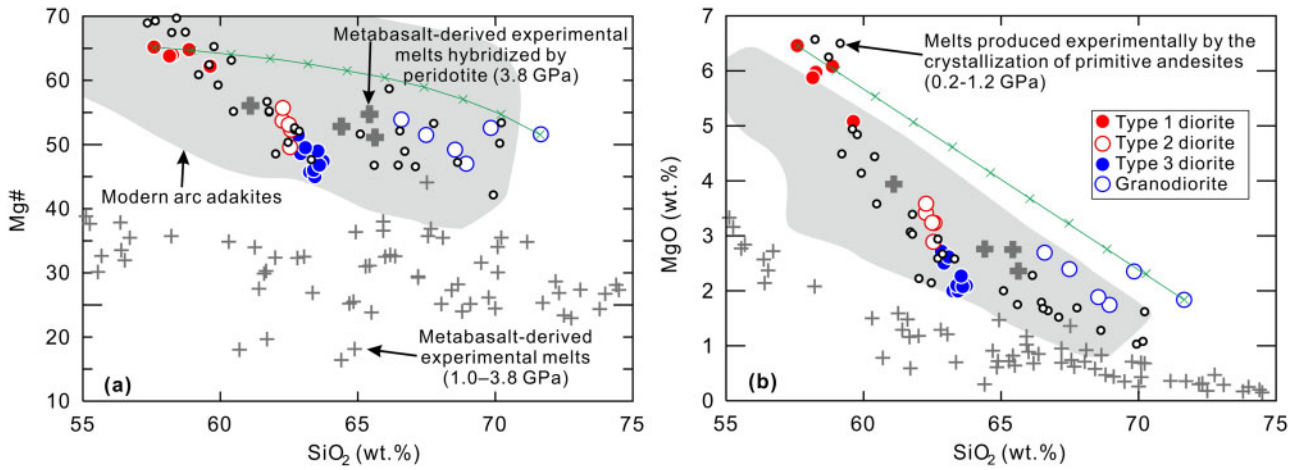

Fig. 3. (a) Mg# vs SiO_2 content. (b) MgO vs SiO_2 content. The data from high-pressure (1·0–3·8 GPa) meta-basalt melting experiments with and without reaction with peridotite are from Sen and Dunn (1994), Rapp and Watson (1995), Rapp *et al.* (1999) and Sisson and Kelemen (2018). The grey field of modern arc adakites was constructed using the compilation of Wang *et al.* (2006). The melts produced experimentally by the crystallization of hydrous primitive andesites are from Müntener *et al.* (2001), Grove *et al.* (2003) and Tatsumi *et al.* (2006). Green lines are models of mixing between the Baohu porphyry samples with the lowest and highest SiO_2 contents, with crosses at 10% intervals. The data for the six granodiorite and three Type 3 diorite samples collected from the western pluton are from Zhai *et al.* (2013).

magnesiohornblende and ferrotschermakite with $(Na + K)^A$ <0·5 apfu (Fig. 7a). Based on the textural and compositional characteristics of the amphibole and its host rocks (Table 1; Fig. 2), the amphibole (hereinafter defined as Type 1 amphibole) in Type 1 diorite can be divided into two types (types 1a and 1 b), and the amphibole (hereinafter defined as Type 3 amphibole) in Type 3 diorite can be divided into three types (3a, 3 b, and 3c). The different amphibole types have distinct major- and trace-element compositions (Fig. 7).

Type 1a amphibole is found in the cores of strongly zoned phenocrysts; Type 1b occurs as small crystals within the matrix, phenocrysts with little to no zoning and the rims of zoned phenocrysts (Fig. 2c). A representative amphibole phenocryst (Fig. 2c) displays simple normal zoning with the high-Mg and high-Al core surrounded by a low-Mg and low-Al rim (Fig. 8a), with the composition of the rim being similar to those of adjacent amphibole microcrysts in the matrix (Fig. 8a). Type 1a amphibole generally has higher MgO, Al_2O_3 (Fig. 7b) but lower REE (Fig. 7d) contents and higher Eu/Eu* ($Eu_N/(Sm_N \times Gd_N)^{1/2}$, where N denotes chondrite-normalized values) and Sr/Sr* ($2Sr_{PM}/(Ce_{PM} + Nd_{PM})$, where PM denotes primitive-mantle-normalized values) ratios (Fig. 7e) than Type 1b amphibole. Normalizing values are from Sun and McDonough (1989). Types 1a and 1 b amphibole have subparallel REE patterns, with the exception of their Eu anomalies (Fig. 7d).

Type 3a amphibole macrocrysts (Fig. 2e, f) and small, anhedral phenocrysts (Fig. 2j) have remarkably homogeneous chemistry (Lines 5 and 8 in Fig. 8a) and embayed edges. Type 3b amphibole occurs as euhedral phenocrysts (Fig. 2i). Small, euhedral amphibole inclusions in large plagioclase phenocrysts are defined as Type 3c amphibole (Fig. 2k). From Type 3a through Type 3b to Type 3c amphibole, HREE are progressively depleted (e.g. with increasing Dy/Yb ratios; Fig. 7f) on chondrite-normalized REE diagrams (Fig. 7c). MgO contents (Fig. 7b) and Eu/Eu* and Sr/Sr* ratios (Fig. 7e) also decrease, but Al_2O_3 contents (Fig. 7b) remain relatively constant.

Garnet major- and trace-element compositions

Garnet phenocrysts are only observed in Types 2 and 3 diorites. All of the analysed garnet is almandine ($Alm_{57–67}Py_{11–25}Gr_{12–22}$) (Alm, almandine; Py, pyrope; Gr grossular) with low spessartine (<5 mol %) contents (Table S5). Garnet from Type 2 diorite has lower Gr (12–16 mol %) but higher Py (20–25 mol %) contents than garnet from Type 3 diorite (Gr =16–22 mol %; Py = 11–13 mol %; Fig. 9a). Garnet compositions within each diorite type are homogeneous, and no significant major-element zonation is observed (Fig. 8b).

Garnet from Type 2 diorite displays strong light REE (LREE) depletion and HREE enrichment (Fig. 9c), and single crystals have limited core-to-rim variations in Yb contents and Dy/Yb ratios (Line 2 in Fig. 8b). In contrast, garnet from Type 3 diorite is characterized by flat to depleted HREE patterns with variable HREE contents (Fig. 9c). For example, Yb contents vary by about three orders of magnitude: 0·08–39·5 ppm. A significant core-to-rim decrease in Yb contents and increase in Dy/Yb ratios occurs in garnet crystals from Type 3 diorite (Lines 4, 6 and 7 in Fig. 8b). The major-element and garnet endmember contents, however, display no visible change (Lines 4, 6 and 7 in Fig. 8b). Overall, garnet from Type 3 diorite has a larger range of HREE contents (Fig. 9c) and higher Dy/Yb ratios (Fig. 9d) than that from Type 2 diorite.

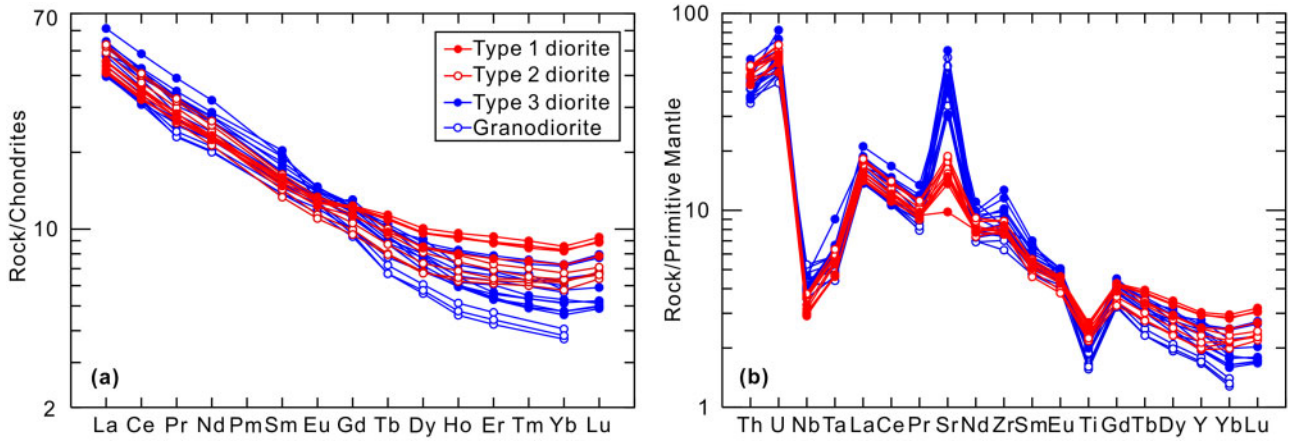

Fig. 4. (a) Chondrite-normalized REE and (b) primitive-mantle-normalized multi-element patterns of the Baohu porphyries. Normalizing values are from Sun and McDonough (1989). The low-concentration Tm and Lu in the granodiorite samples (Zhai *et al.*, 2013) are not shown.

Plagioclase major-element compositions

Plagioclase phenocrysts from Type 3 diorite have remarkably homogeneous geochemistry with a narrow range of An contents (36–41; Table S6). A representative plagioclase phenocryst shows a slight core-to-rim decrease in An contents (Fig. 8c).

DISCUSSION

Origin of almandine garnets in diorite porphyries

Much attention has centered on the origin of almandine garnet in andesites, dacites and their intrusive equivalents (e.g. Green & Ringwood, 1968; Fitton, 1972; Day *et al.*, 1992; Harangi *et al.*, 2001; Yuan *et al.*, 2009; Bach *et al.*, 2012; Shuto *et al.*, 2013; Luo *et al.*, 2018). A global study of garnet-bearing magmatic rocks by Harangi *et al.* (2001) demonstrated that almandine in S-type granites and metapelites has low CaO (<4wt %) and variable MnO contents (Fig. 9b), and is usually associated with quartz, biotite, K-feldspar, plagioclase and cordierite. In contrast, natural and experimental almandine from mantle-derived (M-type) or I-type magmas is characterized by relatively high CaO contents (>4 wt %; Fig. 9b), and often appears with amphibole and plagioclase. Thus, the Ca-rich (>4·3 wt %) and Mn-poor (<2·3 wt %) almandine and coexisting amphibole in the Baohu diorites are consistent with crystallization from M- or I-type magmas (Fig. 9b). The high grossular content (>12 mol %) of the garnet implies high-pressure (>7 kbar) crystallization on the basis of the experimental garnet compositions (Green, 1977, 1992). Primary garnet in andesites from the Northern Pannonian Basin (Harangi *et al.*, 2001), which has similar CaO and MnO contents to our samples, was also thought to have crystallized at high pressures (7–12 kbar) from mantle-derived magmas (Fig. 9b).

Almandine garnet in both types 2 and 3 diorites is interpreted as being a magmatic phase cognate with its host rocks on the basis of the following petrographic and geochemical characteristics.

(1) Garnet crystals in Type 3 diorite are commonly intergrown with plagioclase phenocrysts. Fig. 2g shows that an irregular, anhedral garnet crystal included in a large plagioclase phenocryst also contains small plagioclase grains in its rim, and these plagioclase inclusions have the same compositions and optical orientations as the host plagioclase core (Fig. 2g), indicating that the rim of this garnet inclusion and the host plagioclase phenocryst crystallized simultaneously from the host melt.

(2) Consistent correlation between garnet and whole-rock compositions suggests that the latter reflects the overall composition of the bulk magma from which the garnet crystallized. For example, garnet in Type 3 diorite has lower MgO and higher CaO contents and Dy/Yb ratios than that in Type 2 diorite (Fig. 9b, d), a difference also shown by their corresponding host rocks (Fig. 5b, c). The compositions of garnet xenocrysts entrained from unrelated crustal lithologies cannot vary regularly with those of their host rocks. In addition, the most likely sources of xenocrystic garnet are the Triassic Pianshishan eclogites and blueschists (the red star in Fig. 1a) exposed 60 km southwest of the Baohu diorites, but metamorphic garnet from these rocks is characterized by higher grossular garnet and lower pyrope contents than that found in the diorites (Fig. 9a) due to their high-pressure (2·0–2·5 GPa) and low-temperature (410 °C–460 °C) metamorphic conditions (Zhai *et al.*, 2011).

(3) Zircon crystals in Type 3 diorite also have higher Dy/Yb ratios and a larger range in Dy/Yb ratios than those in Type 2 diorite (Fig. 6f). The average HREE partition coefficients between zircon and garnet in each diorite type fall between those measured in experiments at 850 °C and 900 °C (Fig. 10; Rubatto & Hermann, 2007); therefore, the HREE patterns of the garnet are consistent with their crystallization in equilibrium with the magmatic zircon.

Almandine in the Baohu diorite porphyries was crystallized from an andesitic host magma at relatively high

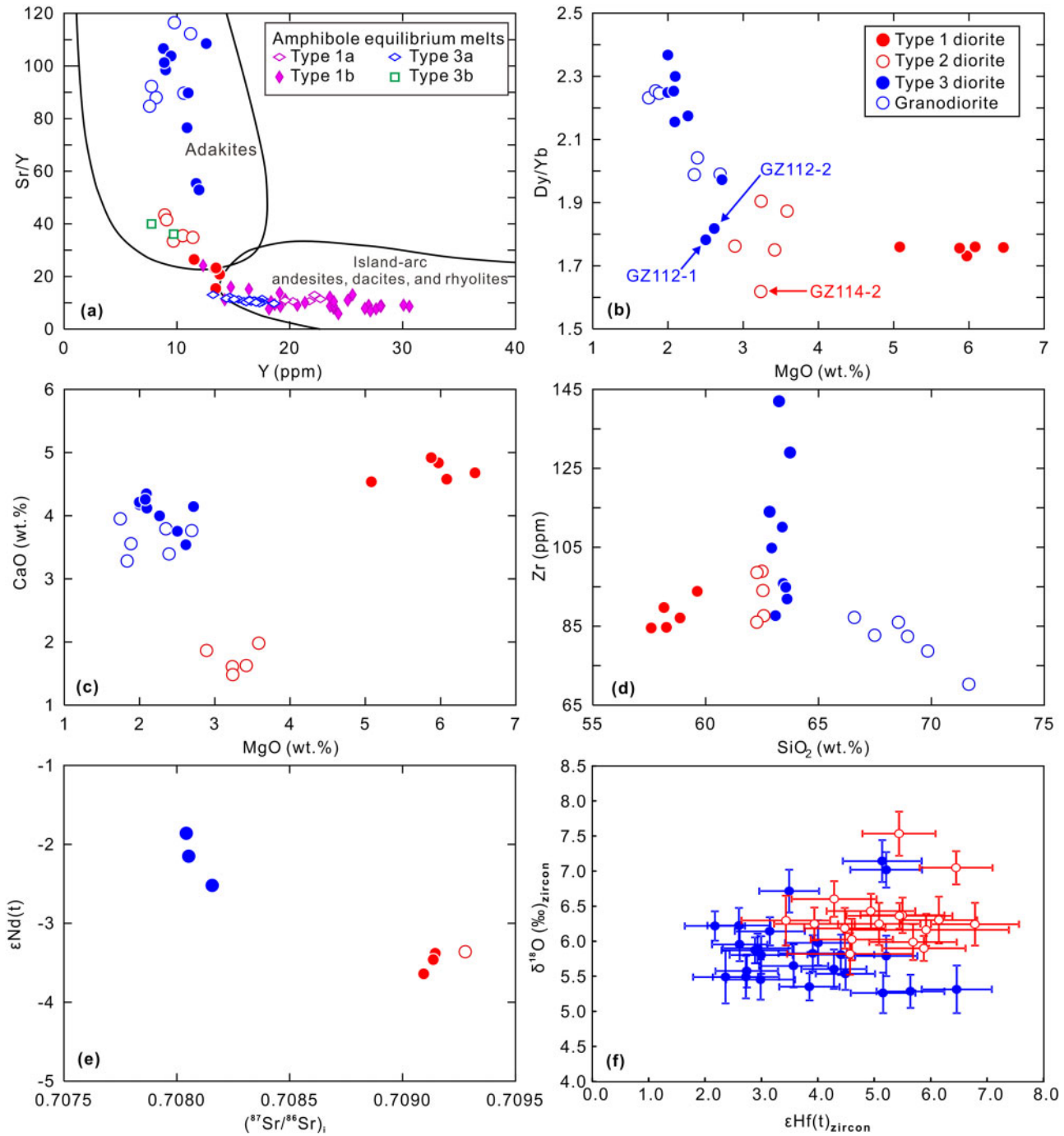

Fig. 5. (a) Sr/Y vs Y diagram (after Defant & Drummond, 1990). (b) Dy/Yb vs MgO diagram. (c) CaO vs MgO diagram. (d) Zr vs SiO_2 diagram. (e) Whole-rock Sr–Nd isotopic compositions. (f) Zircon Hf–O isotopic compositions. The trace-element compositions of amphibole equilibrium melts in (a) were calculated using partition coefficients from the multiple-regression model of Humphreys *et al.* (2019).

pressure (>7 kbar). This Ca-rich garnet is unstable at low pressures (i.e. the emplacement depth of porphyries), where it was no longer in equilibrium with the host magma and began to resorb and react to form different phases (Green & Ringwood, 1968; Day *et al.*, 1992; Harangi *et al.*, 2001). The garnet in Type 3 diorite, especially those crystals that were not protected from reacting with the host melt by plagioclase phenocrysts, have embayed edges and reaction coronas of fine-grained, interlocking plagioclase + amphibole (chlorite alteration) ± oxides (Fig. 2h); a garnet consumption reaction consistent with experimental results (Alonso-Perez *et al.*, 2009). Experimentally produced magmatic garnet shows consistent evolutionary trends, with increasing almandine and grossular contents with decreasing temperature (Fig. 9a; Alonso-Perez *et al.*

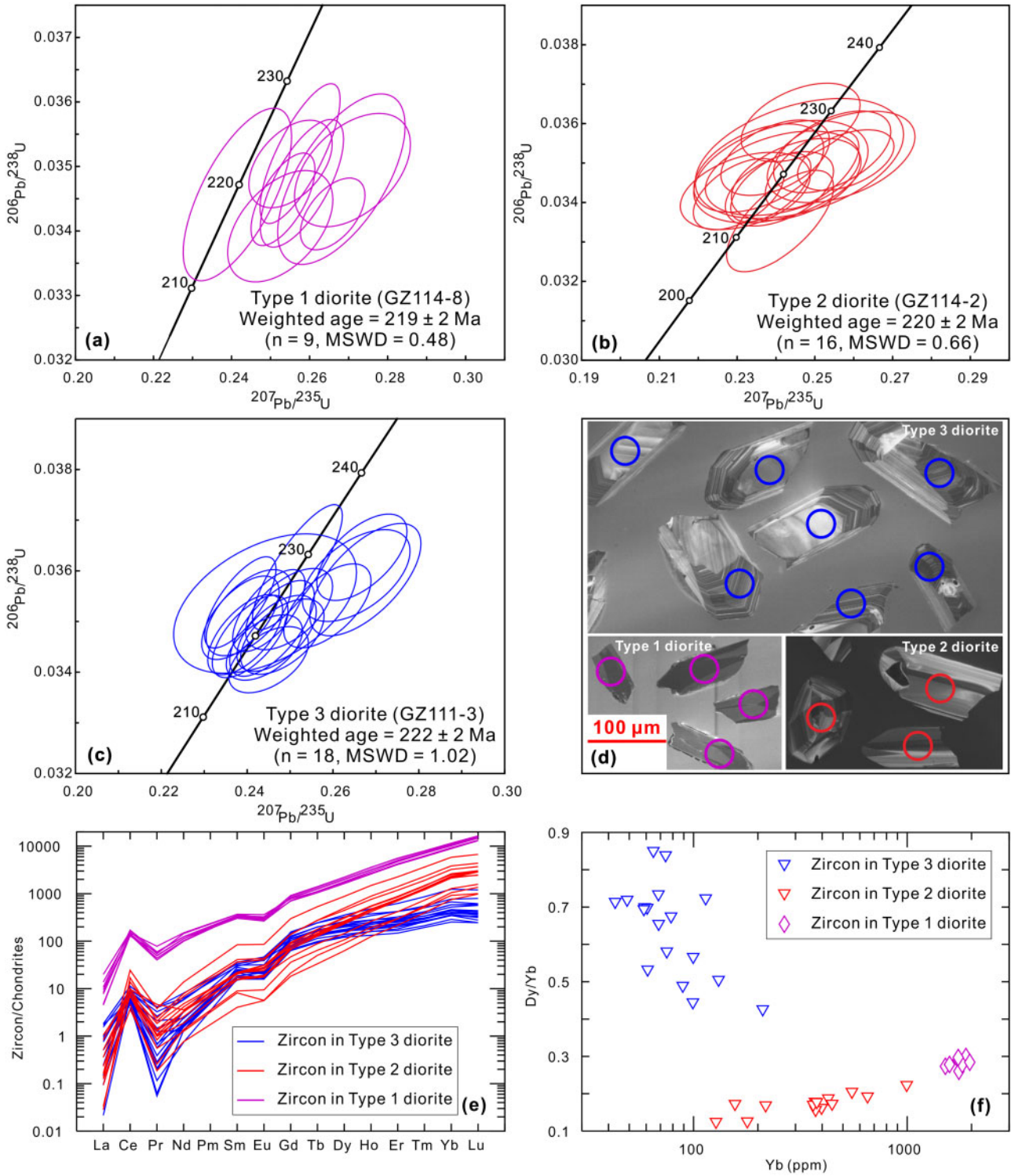

Fig. 6. LA–ICP–MS zircon U–Pb concordia diagrams for (a) Type 1, (b) Type 2 and (c) Type 3 diorites. (d) Representative zircon CL images. Circles in CL images denote the analysis spots. (e) Chondrite-normalized REE patterns of zircon. (f) Zircon Dy/Yb v s Yb diagram. Normalizing values are from Sun and McDonough (1989).

2009; Ulmer *et al.* 2018). The compositions of garnet from Type 2 diorite, with higher MgO and lower CaO contents than garnet from Type 3 diorite, may, therefore, reflect crystallization from a more primitive magma.

Early-crystallizing garnet did not necessarily separate from rapidly rising magma. Garnet from Type 3 diorite shows a significant core-to-rim decrease in Yb contents and increase in Dy/Yb ratios (Lines 4, 6 and 7 in Fig. 8b), reflecting crystallization of garnet rims from

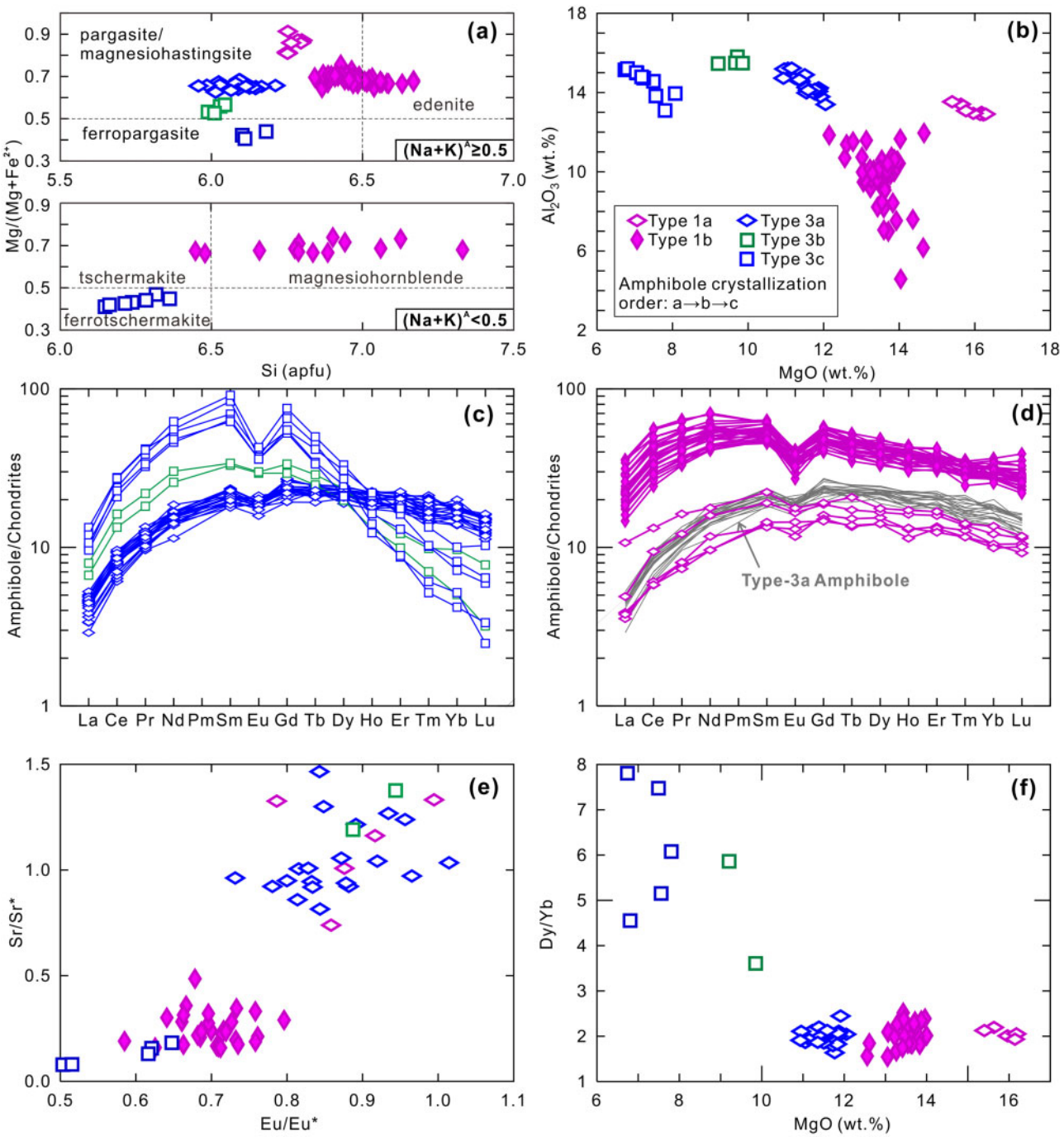

Fig. 7. Major- and trace-element compositions of amphibole from Type 1 and Type 3 diorite. (a) Classification diagram for calcic amphibole with $Ca_B \geq 1{\cdot}50$ and $Ti > 0{\cdot}50$. (b) Al_2O_3 vs MgO diagram. Chondrite-normalized REE patterns of amphiboles from (c) Type 3 and (d) Type 1 diorite. (e) Amphibole Sr/Sr* vs Eu/Eu* diagram. (f) Amphibole Dy/Yb vs MgO diagram.

a melt depleted in HREE by earlier garnet fractionation. The Dy/Yb ratio increases significantly with the decreasing MgO contents of the different amphibole types in the Type 3 diorites (Fig. 7f), suggesting that these amphibole crystals were also derived from a melt that became progressively depleted in HREE. The host Type 3 diorites and granodiorites show an increase in whole-rock Dy/Yb ratios with decreasing MgO contents (Fig. 5b), further indicating that the Type 3 diorites experienced both garnet crystallization and garnet fractionation. Garnet crystals from Type 3 diorite display no significant major-element zoning, but large differences in the Yb contents of the cores and rims (Lines 4, 6 and 7; Fig. 8b). Diffusion may have smoothed slight changes in major-element contents without changing the REE profiles inherited from the magma, as the diffusion rates of REE^{3+} in garnet are significantly slower than those of divalent cations (e.g. Mg^{2+}, Ca^{2+} and Fe^{2+},

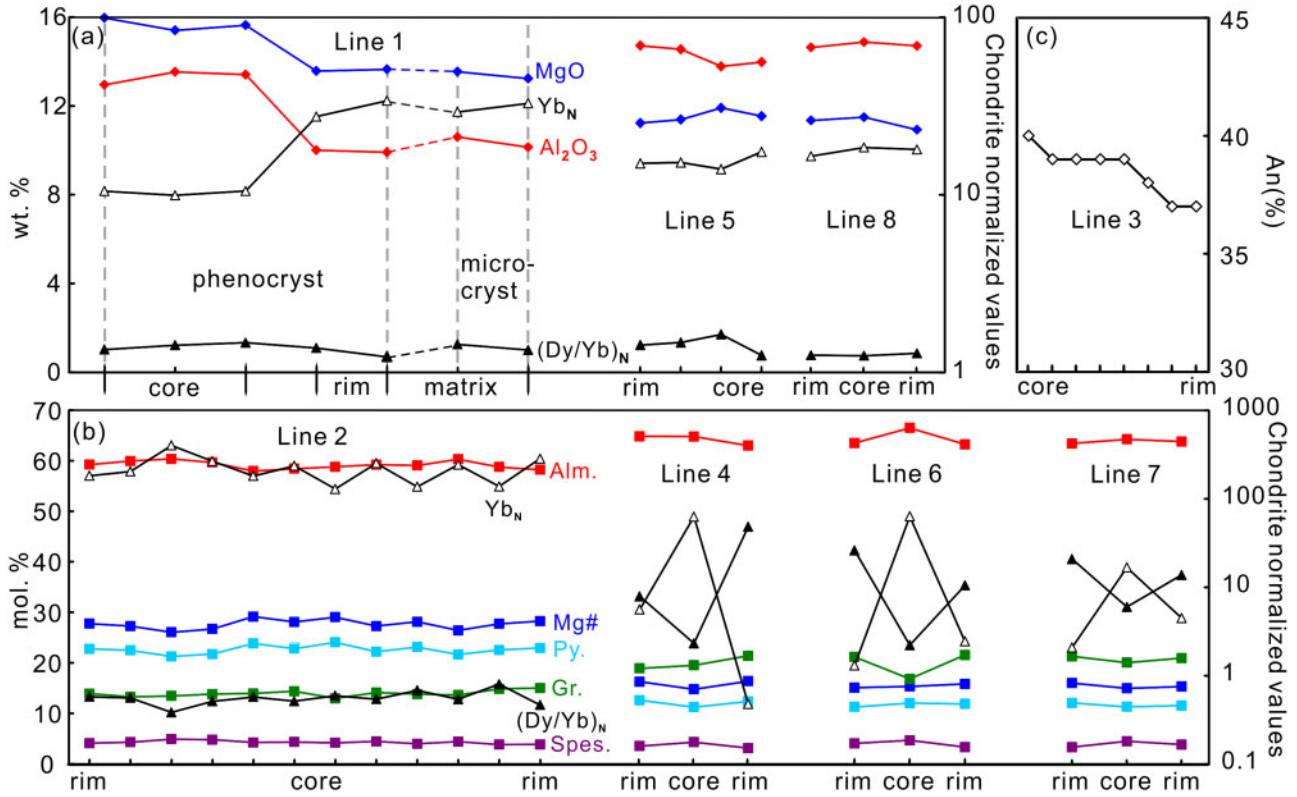

Fig. 8. Compositional profiles of (a) amphibole, (b) garnet and (c) plagioclase. The locations of the profiles are shown by the yellow lines in Fig. 2. Lines 3 and 5 are core-to-rim profiles, and lines 2, 4, 6, 7 and 8 are rim-to-rim traverses. Note that line 1 passes through the core and rim of a zoned amphibole phenocryst and then passes into the adjacent amphibole microcryst. Alm, almandine; Py, pyrope; Gr, grossular; Spes, spessartine.

Lanzirotti, 1995; Van Orman *et al.*, 2002). In contrast, garnet crystals in the Type 2 diorites are larger and lack reaction coronas of plagioclase and amphibole (Fig. 2d), suggesting a shorter residence time in the magma chamber. The lack of Yb zoning in the garnet (Line 2 in Fig. 8b), and the narrow range of whole-rock Dy/Yb ratios (Fig. 5b), also implies there was little time for most of garnet to separate from the host magma.

Pressure and temperature conditions

In addition to Ca-rich almandine garnets, we further provide the following constraints on the pressures and temperatures under which the andesitic magmas crystallized and differentiated.

Constraints from amphibole compositions

The Type 3a amphibole occurs as anhedral macrocrysts and phenocrysts, both of which are characterized by disequilibrium and dissolution features such as embayed edges and resorption channels (Fig. 2e, f, j). The Type 3a amphibole has nearly flat HREE patterns (Fig. 7c), with lower Dy/Yb ratios ($1{\cdot}98 \pm 0{\cdot}18$) than its host rock (sample GZ111-3; Dy/Yb = 2·25). In theory, an amphibole crystal should have a higher Dy/Yb ratio than its equilibrium melt, as Dy is more compatible than Yb in amphibole (Tiepolo *et al.*, 2007). Therefore, the anhedral Type 3a amphibole can be best described as antecrysts (Davidson *et al.*, 2007) that did not crystallize from the evolved host magma, but may have grown in more primitive parental magmas with higher MgO contents and lower Dy/Yb ratios, similar in composition to the other two Type 3 samples (GZ112-1 and GZ112-2; Fig. 5b).

Amphibole compositions are widely used to calculate crystallization temperatures and pressures. We chose two amphibole-only geobarometers (Krawczynski *et al.*, 2012; Ridolfi and Renzulli, 2012). Temperature was calculated using the geothermometers of Ridolfi and Renzulli (2012) and Putirka (2016). The close agreement of the temperatures (~719–975 °C; Table S4) obtained with the two geothermometers (Supplementary Data Fig. S1b) indicates that amphibole compositions are sensitive to temperature and that the temperature estimates are reasonable (Erdmann *et al.*, 2014; Putirka, 2016). The different amphibole types within each diorite type have different crystallization temperatures, indicating that amphibole Type (1, 3) a crystallized first, followed by Type b and then Type c (Fig. S1b). However, the two geobarometers give significantly different pressure values, especially for some Type 3 amphibole crystals, even given the relatively large error of the geobarometers (Fig. S1a).

To choose the most reasonable pressure estimates, we studied the substitution mechanisms in the Baohu

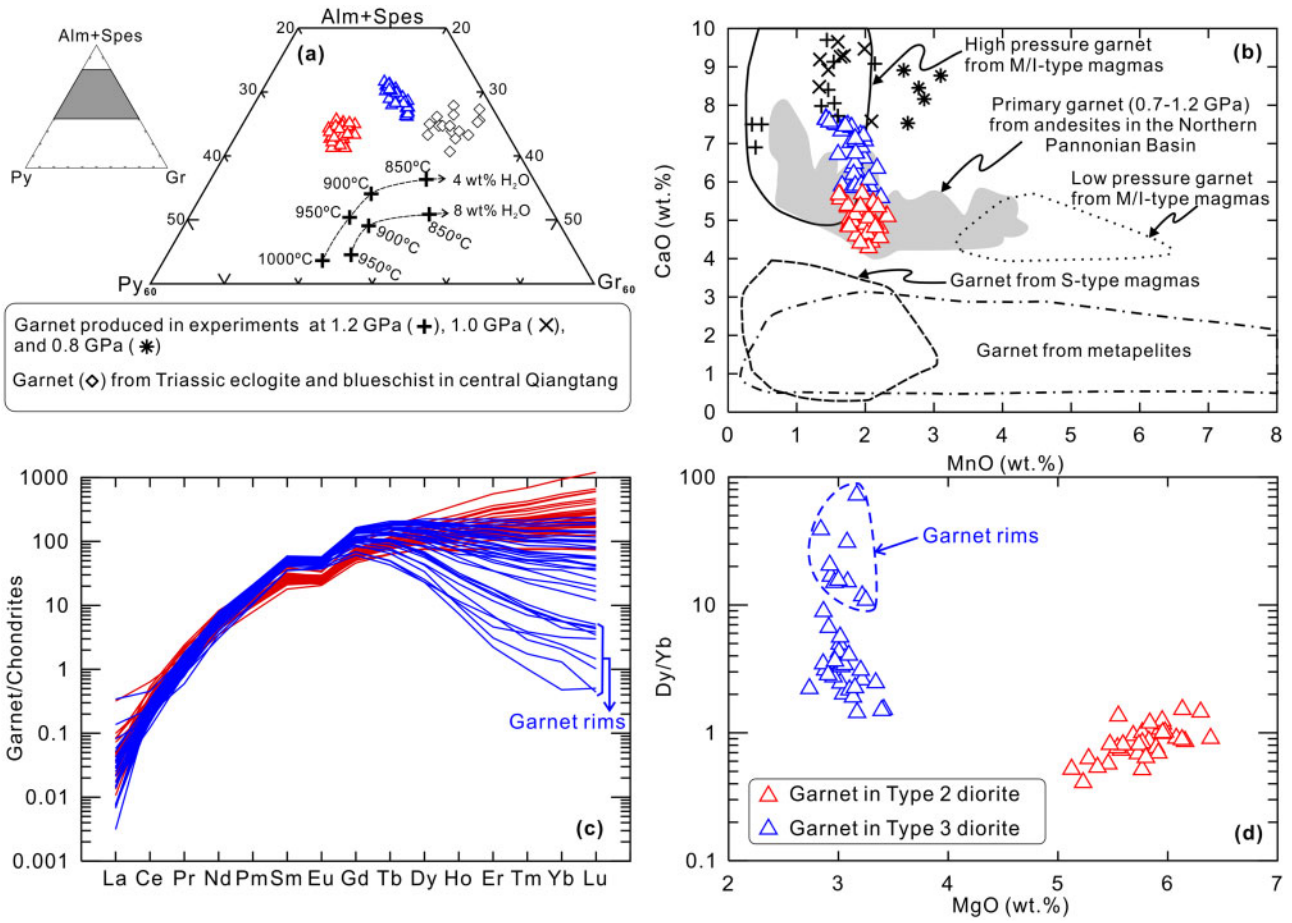

Fig. 9. Major- and trace-element compositions of garnet from Type 2 and Type 3 diorite. (a) Garnet endmember compositions. The two arrows illustrate isobaric (1·2 GPa) cooling trends for andesitic magmas with 4 and 8 wt % H_2O (Alonso-Perez *et al.*, 2009). The data for garnet from the Triassic eclogites and blueschists in central Qiangtang are from Zhai *et al.* (2011) and (Zhang et al., 2006) . (b) Garnet CaO vs MnO diagram. Garnet composition fields from Harangi *et al.* (2001). Experimental garnet from andesitic and basaltic magmas at 1·2, 1·0 and 0·8 GPa are from Müntener *et al.* (2001), Alonso-Perez *et al.* (2009) and Ulmer *et al.* (2018). (c) Chondrite-normalized garnet REE patterns. (d) Garnet Dy/Yb vs MgO diagram. Normalizing values are from Sun and McDonough (1989). Note that the rims of the garnet in the Type 3 diorites have higher Dy/Yb ratios and lower Yb contents than their cores.

amphibole, including the pressure-sensitive Al-tschermakite and temperature-sensitive Ti-tschermakite and edenite substitutions (e.g. Bachmann & Dungan, 2002; Kiss *et al.*, 2014). The positive correlation between Al^{IV} and $(Na + K)^A$ within each diorite type indicates significant temperature control on composition (Fig. 11a). The correlation between Al^{IV} and Ti is stronger in Type 3 amphibole than that in Type 1 amphibole (Fig. 11b), meaning that the compositional variations in Type 3 amphibole are more strongly controlled by temperature. In contrast, the compositional variations within Type 1 amphiboles are likely to be affected by variations in the melt chemistry in addition to temperature and pressure. The wide range of Si and Al contents of Type 1 amphibole (Fig. 7a, 11) also supports this inference, as amphibole Si–Al composition is strongly correlated with melt composition (Sisson & Grove 1993; Erdmann *et al.*, 2014). Low-temperature amphibole that crystallizes from felsic magma tends to have higher Si contents but lower Al^{IV} contents and $Mg/(Mg + Fe^{2+})$ ratios than high-temperature amphibole that crystallizes from more mafic magmas (Erdmann *et al.*, 2014; Kiss *et al.*, 2014). Therefore, the Type 1a amphibole may have crystallized from hotter, more primitive magmas than the Type 1b amphibole, consistent with the geothermometry (Fig. S1b) and the observation that the former occurs only in the core of the latter (Fig. 2c). Their different Al_2O_3 contents cannot be explained only by crystallization at different pressures, but rather reflects significant variations in magma composition.

Type 3 amphibole has higher Al^{IV} contents and lower $Mg/(Mg + Fe^{2+})$ ratios than Type 1 amphibole (Fig. 11d), suggesting that the different Al_2O_3 contents of the two types may be due mainly to differences in crystallization pressure, rather than in magma composition (e.g. Kiss *et al.*, 2014). In addition, there is no significant correlation between Al^{IV} and Al^{VI} contents within each diorite type (Fig. 11c), indicating limited pressure control. However, significant differences in Al^{IV} and Al^{VI} contents between diorite types (Fig. 11c) suggest a difference in crystallization pressures, with Type 1 amphibole crystallizing at lower pressures than

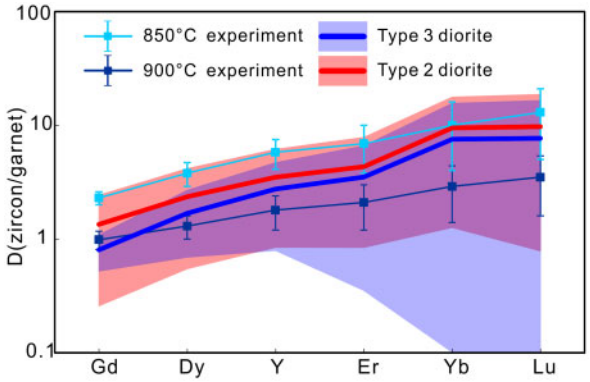

Fig. 10. HREE partition coefficients between zircon and garnet from the Type 2 and Type 3 diorites. Experimentally determined zircon/garnet partition coefficients (with 1SD error bars) at 850 °C and 900 °C are shown for comparison (Rubatto & Hermann, 2007). The coloured solid lines and shaded areas are the average partition coefficients and their standard deviations calculated from our samples, respectively. The large standard deviation for Type 3 diorite results from the large variation in HREE contents of their garnets.

Type 3 amphibole. However, the pressure estimates obtained using the geobarometer of Ridolfi and Renzulli (2012) indicate that Type 1a amphibole crystallized at a higher pressure than Type 3 amphibole (Fig. S1a). Moreover, the pressures (607 ± 155 MPa) calculated for Type 3 amphibole are inconsistent with the pressures inferred from the mineral crystallization order (see next Section). Thus, we prefer the pressures calculated using the Al^{VI}-in-amphibole geobarometer of Krawczynski *et al.* (2012), although it might not accurately estimate the crystallization pressures of Type 1 amphibole where variations in magma composition, rather than in pressure, are the main control on the Al content.

The relative pressure estimates between the different amphibole populations can be further verified by comparing the composition of Baohu amphibole to that of amphibole produced experimentally in andesitic and dacitic melts at 220–1200 MPa (Scaillet & Evans, 1999; Prouteau & Scaillet, 2003; Alonso-Perez *et al.*, 2009). We selected only amphibole that crystallized from intermediate to felsic starting materials to evaluate the effects of pressure and temperature, rather melt composition, on amphibole composition. Crystallization experiments show that the Al and Na + K contents of amphibole vary with pressure and temperature, and that their compositions plot in distinct pressure-dependent compositional fields (Fig. 12a). Type 1a and Type 3 amphibole are characterized by high Al contents, and cluster in the 800, 960 and 1200 MPa fields (Fig. 12a). In contrast, the Type 1b amphibole has lower Al contents, and mostly falls in the 220 and 400 MPa fields (Fig. 12a). Some natural amphibole does not strictly fall within these compositional fields, with lower Na + K contents (Fig. 12a), perhaps indicating formation at lower temperatures (Prouteau & Scaillet, 2003). These semi-quantitative results are consistent with the previous pressure estimates obtained using the geobarometer of Krawczynski *et al.* (2012).

Constraints from crystallization sequence of minerals

According to the experimental results compiled by Ridolfi *et al.* (2010), amphibole with high Al# values ($Al^{VI}/Al_{total} > 0{\cdot}21$) is often in equilibrium with experimental melts with high water contents (4·5–13·0 wt %; mean = 8·3 wt %) at high pressures. All Type 3 amphibole has high Al# values (0·23 ± 0·03). Calculated melt H_2O contents by using the amphibole hygrometer of Ridolfi *et al.* (2010) are 8·7 ± 0·3 wt % for Type 3 diorites and 5·8 ± 0·6 wt % for Type 1 diorites (Table S4). In addition, application of the plagioclase-liquid hygrometer (Waters & Lange, 2015) to Type 3 diorites results in melt H_2O contents of 7·0 ± 0·1 wt %. In Type 3 diorites, the key temperature parameter of the plagioclase-liquid hygrometer can be constrained by the crystallization temperature of Type 3c amphibole (Table S6). Therefore, a phase equilibrium diagram for andesitic melts with an H_2O content of 5 wt % (Green, 1982) can be used to further constrain the temperature and pressure of the mineral assemblages observed in the Baohu diorites.

The order that minerals in the Baohu diorites crystallized can be determined from the trace-element contents of different amphibole types that crystallized during different stages. In the garnet-bearing Type 3 diorites, the Type 3a amphibole has no significant Eu anomalies and flat HREE patterns (Fig. 7c), indicating that it crystallized before plagioclase and garnet. Type 3b amphibole has similar Eu/Eu* and Sr/Sr* ratios (Fig. 7e) to Type 3a amphibole but highly fractionated HREE patterns (Fig. 7c), indicating that it crystallized before plagioclase but at the same time as garnet. The small Type 3c amphibole crystals included in large plagioclase phenocrysts have the lowest Eu/Eu* and Sr/Sr* ratios of the Type 3 amphibole (Fig. 7e), and strongly depleted HREE patterns (Fig. 7c), indicating that Type 3c amphiboles crystallized at the same time as plagioclase and either at the same time as or after garnet. Given that quartz occurs mainly in the fine-grained matrix, the order in which minerals in the Type 3 diorites first began to crystallize is amphibole, garnet, plagioclase, and then quartz. The first appearance of garnet before plagioclase but after amphibole suggests that the *P–T* path of the magma during cooling and crystallization passed through the solid blue line in the phase-equilibrium diagram (Fig. 12b), and that the parent magma of Type 3 diorite underwent crystallization and differentiation at 900–1200 MPa. The crystallization pressure (928 ± 156 MPa) of Type 3 amphibole estimated using the geobarometer of Krawczynski *et al.* (2012) matches this inferred pressure range. Overall, the geothermobarometers and phase-equilibrium diagram reveal an isobaric cooling and fractionation trend

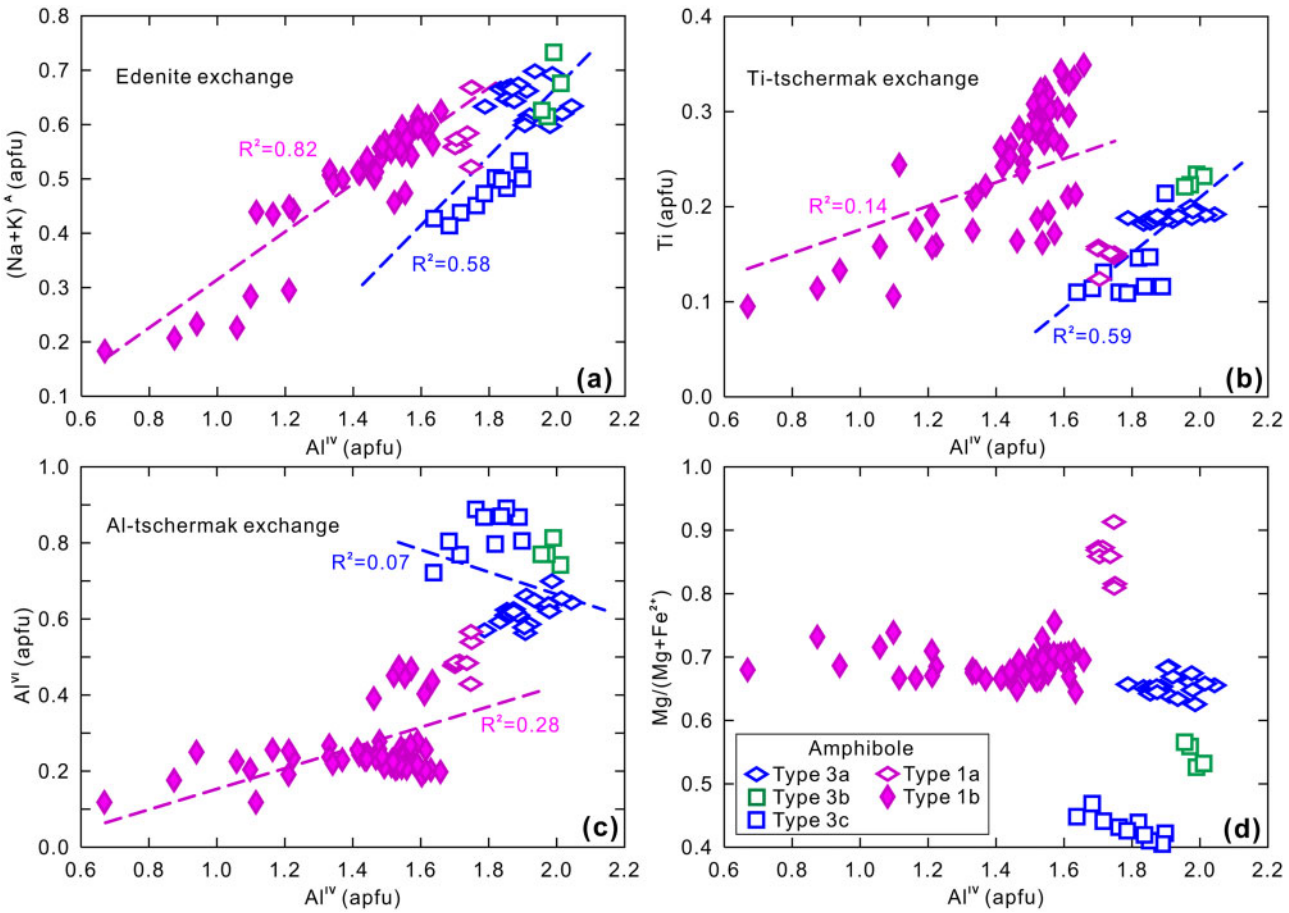

Fig. 11. Al^{IV} vs (a) $(Na + K)^{A}$, (b) Ti and (c) Al^{VI} diagrams illustrating exchange mechanisms in the Baohu amphibole. Regression lines were calculated for each diorite type. (d) $Mg/(Mg + Fe^{2+})$ vs Al^{IV} diagram. All values are in apfu.

(the dashed blue arrow in Fig. 12b) at a pressure of ~1 GPa.

In the Type 1 diorites, Type 1a amphibole has no significant Eu anomalies (Fig. 7d), indicating that it crystallized before plagioclase. Although Type 1b amphibole rims have flat HREE patterns similar to that of the Type 1a amphibole present in their cores (Fig. 7d), they are characterized by larger negative Eu and Sr anomalies (Fig. 7d, e), suggesting that Type 1b amphibole and plagioclase crystallized simultaneously, with garnet not crystallizing while the Type 1 amphibole was crystallizing. There are also no garnet phenocrysts found in the Type 1 diorites and no garnet inclusions in the early-crystallized amphibole. The first appearance of plagioclase after amphibole suggests that the *P–T* path of the magma during ascent passed through the solid red line in the phase-equilibrium diagram (Fig. 12b), implying that crystallization began at 500–900 MPa. The *P–T* estimates for Type 1 amphibole suggest that the Type 1 diorites followed a simultaneous cooling and depressurization path, as shown by the dashed red arrow in Fig. 12b. Some Type 1b amphibole crystals plot outside the amphibole stability field because the Al^{VI}-in-amphibole geobarometer underestimated their crystallization pressures.

Generation of high-Mg# adakitic rocks through lower-crustal magma differentiation

The Baohu adakitic diorites cannot have been directly generated by lower crustal melting (e.g. Atherton & Petford, 1993; Wang *et al.*, 2005), as they have higher MgO contents and Mg# values than liquids produced by the experimental melting of metabasalt at 1·0–3·8 GPa (Fig. 3; Sen & Dunn, 1994; Rapp & Watson, 1995; Sisson & Kelemen, 2018), but their compositions are similar to those of liquids produced in experiments where metabasalt-derived melt reacts with peridotite (Fig. 3; Rapp *et al.*, 1999). Experimental data compiled by Kelemen (1995) also show that most liquids produced by melting basalt at pressures of 1 bar to 30 kbar with SiO_2 contents of >55 wt % have Mg# values of <33.

Furthermore, the Baohu adakitic diorites could not have been generated by mixing of mantle-derived and adakitic crustal melts (e.g. Streck *et al.*, 2007): first, magma mixing is commonly accompanied by oscillatory or reverse zoning of phases such as plagioclase, amphibole, and garnet (e.g. Harangi *et al.*, 2001; Bach *et al.*, 2012; Ribeiro *et al.*, 2016) but these minerals are either homogeneous or have simple normal zoning (Fig. 8); second, mixing in the Baohu area would imply

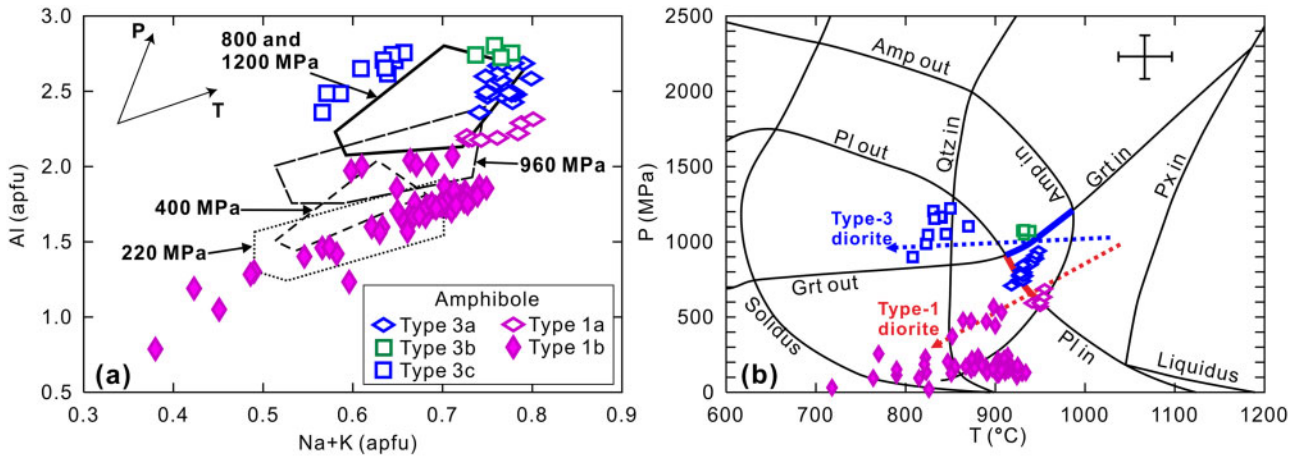

Fig. 12. (a) Al vs (Na + K) diagram of the Baohu amphibole and amphibole crystallized in dacitic and andesitic melts in experiments at 220, 400, 800, 960 and 1200 MPa (Scaillet & Evans, 1999; Prouteau & Scaillet, 2003; Alonso-Perez *et al.*, 2009). The arrows illustrate the potential effect of pressure (*P*) and temperature (*T*) on amphibole compositions. (b) Pressure and temperature estimates for amphibole from Type 1 and Type 3 diorite plotted on a phase diagram for andesite with 5 wt % H_2O (Green, 1982). Pressure and temperature were calculated using the geobarometer of Krawczynski *et al.* (2012) and geothermometer of Putirka (2016). Uncertainty bars in the upper right corner indicate representative errors in the geothermobarometry. The dashed blue and red arrows are potential evolutionary paths for the garnet-bearing Type 3 diorites and the garnet-free Type 1 diorites, respectively. The solid blue and red lines show the crystallization pressure range of the parental magmas of the Type 3 and Type 1 diorites, respectively, as inferred from the mineral crystallization order. Px, pyroxene; Qtz, quartz; Pl, plagioclase; Amp, amphibole; Grt, garnet.

that the types 2 and 3 adakitic diorites were derived by mixing of granodiorite with adakitic affinity and Type 1 diorite with Mg# values > 60 (the only candidates for crust- and mantle-derived endmembers, respectively). However, the Baohu diorites and granodiorites display curved chemical trends on binary diagrams, deviating from trends formed by magma mixing (green lines in Fig. 3); and the CaO–MgO plot indicates that Type 2 diorites cannot have been produced by mixing of granodiorite and Type 1 diorite (Fig. 5c). The transition from increasing to decreasing Zr content with increasing SiO_2 content can be explained by zircon fractionation at high SiO_2 contents (>65 wt %; Fig. 5d), rather than by magma mixing. Zircon fractionation could partially contribute to the HREE depletion in the granodiorites, but not in the diorites with SiO_2 contents of <65 wt % (Fig. 5d). Three samples with the highest Zr (114–142 ppm) contents in Type 3 diorites are from Zhai *et al.* (2013), and they also show positive Zr anomalies (Fig. 4b), implying zircon accumulation.

Finally, if the Baohu high-Mg# adakitic diorites represent pristine magmas produced by interaction between melts derived from eclogitic crust (including subducted slab, eroded forearc crust and delaminated lower continental crust) and peridotite in the mantle, or by lower crustal melting, the melt compositions in equilibrium with the high-pressure, early-crystallized amphibole should show adakitic characteristics (e.g. Ribeiro *et al.*, 2016; Tang *et al.*, 2017). Humphreys *et al.* (2019) developed a multiple-regression model from a database of experimental amphibole that linked trace-element partition coefficients to amphibole major-element chemistry, which we used here to calculate partition coefficients for the Baohu amphibole. The melts calculated to be in equilibrium with the Type 3a amphibole, which crystallized prior to garnet, are characterized by low Sr/Y ratios and high Y contents relative to those in equilibrium with the Type 3b amphibole that crystallized after garnet (Fig. 5a). The former, however, plots outside of the field of typical adakites in the Y–(Sr/Y) diagram (Fig. 5a). Given that the Type 3 diorites underwent garnet fractionation, it is likely that the adakitic whole-rock compositions were produced by the fractionation of garnet and other minerals in the deep crust.

The Type 1 diorites have lower Sr/Y and Dy/Yb ratios and SiO_2 contents, and higher MgO contents than the Type 3 diorites (Fig. 5); the early-crystallized Type 1a and 3a amphibole have similar REE patterns (Fig. 7d). Therefore, the Type 1 diorites could represent the parental magma of the Type 3 diorites. The Type 1 diorites have major element compositions similar to primitive andesites, which are likely produced by melting of strongly hydrated mantle peridotite at low pressures (1·0–2·0 GPa; Wood & Turner, 2009; Mitchell & Grove, 2015). Using natural samples and previous experiments at pressures of 0·2–1·2 GPa, Wang *et al.* (2018a) concluded that the fractional crystallization of mantle-derived primitive andesites can produce andesitic to dacitic arc lavas with relatively high Mg# values of 45–60, as the derived melts inherit high Mg/Si ratios from their parental magma (Fig. 3).

Crystallization experiments performed by Müntener *et al.* (2001), Ulmer *et al.* (2018) and Grove *et al.* (2003) investigated the liquid lines of descent and phase relations for a primitive basaltic andesite at pressures of 1·2, 1·0 and 0·2 GPa, respectively. These experiments provide a reference for determining the fractionating mineral assemblages and crystallization pressures of the Baohu diorites by the pseudo-ternary olivine–clinopyroxene–quartz diagram (Fig. 13), although the Type 1

diorites are slightly evolved relative to the experimental starting material. The liquids produced at 0·2 GPa remain metaluminous (with a positive clinopyroxene component) as a result of the crystallization of olivine, clinopyroxene, plagioclase and minor amphibole. In contrast, the fractionation of pyroxene, amphibole and garnet without olivine and plagioclase at 1·0 and 1·2 GPa drives residual liquids towards andesitic to dacitic corundum-normative compositions. The order in which the minerals in the Type 3 diorites first appear is also consistent with the experiment at 1·0 GPa; therefore, it is possible that the Type 3 diorites, with corundum-normative compositions, were generated by the fractionation of garnet, amphibole, and pyroxene from the Type 1 diorites at ~1·0 GPa. The experiment at 1·.2 GPa produced more clinopyroxene and less orthopyroxene than that at 1·0 GPa, and resulted in residual liquids with lower normative clinopyroxene contents (Fig. 13). Thus, the Type 2 diorites may have been derived from either Type 1 diorite by the fractionation of more clinopyroxene at high pressure (>1·2 GPa) or from a parental magma with lower CaO contents than the basaltic andesite. In summary, peraluminous andesitic melts are not necessarily the result of assimilation of pelitic crustal lithologies or melts by mantle-derived magmas (e.g. Hildreth & Moorbath, 1988). The low zircon $\delta^{18}O$ values (5·9‰ ± 1·0‰ for Type 3 diorite; 6·3‰ ± 0·8‰ for Type 2 diorite) also rule out the assimilation of metasedimentary rocks.

We estimated the proportions of fractionating minerals by the least-squares mass-balance model of Cabero *et al.* (2012) using whole-rock and mineral major-element compositions. The modelling excludes K_2O and Na_2O because of the potential influence of hydrothermal alteration. The best fit results of the modelling (Table S10) show that the Type 1 diorites can produce a daughter magma that is a good match with the average composition of Type 3 diorites by 18% fractionation of garnet, orthopyroxene, and amphibole at a 13:28:59 ratio. If Type 1 diorites are also considered as the parental magmas of Type 2 diorites, the average composition of the latter can be achieved by 24% fractionation of garnet, clinopyroxene, and amphibole at a 7:34:59 ratio. Whether the pyroxene coexisting with garnet is clinopyroxene and/or orthopyroxene depends on pressures (Fig. 13) and water contents. A high pressure (>10 kbar with 5 wt % H_2O; >15 kbar with 3 wt % H_2O) will suppress orthopyroxene but enhance clinopyroxene crystallization (Green, 1992). The fractionating mineral assemblage for Type 3 diorites contains more garnet than that for Type 2 diorites. This is in agreement with observation that Type 3 diorites have higher Dy/Yb ratios than Type 2 diorites (Fig. 5b), and that garnet grains in Type 3 diorites show more significant Yb zoning than those in Type 2 diorites (Fig. 8b).

It is reasonable to consider Type 1 diorites as the parental magmas of Type 2 diorites because they were sampled from the same pluton (Fig. 1b) and have similar Sr–Nd isotopic compositions (Fig. 5e). However, the Type 3 diorites and granodiorites were sampled from a different pluton located ~4 km to the west of the types 1 and 2 diorites (Fig. 1b) and the former has more depleted Sr–Nd isotopic ratios than the latter (Fig. 5e). This difference can be explained by the assimilation of isotopically depleted, juvenile crustal material, such as earlier subduction-related acid rocks (e.g. Wang *et al.*, 2018b; Dan *et al.*, 2019). Nonetheless, all samples display curved chemical trends on binary diagrams (Fig. 3 and 5c–d), indicating that crustal contamination is less important than fractional crystallization. This is further supported by the partially overlapping ranges of zircon O and Hf isotopic ratios (Fig. 5f) of the Types 2 and 3 diorites. Thus, Type 3 diorites may be mainly derived from Type 1 diorites by fractional crystallization, with a secondary role of crustal contamination and the entrainment of a few recycled antecrysts (e.g. highly corroded amphibole macrocrysts). Although the proportions of fractionating minerals estimated based on the whole-rock compositions alone may be biased due to an open system process, the important role of garnet fractionation in the generation of HREE-depletion signatures of the Type 3 diorites is undoubted because this conclusion was mainly drawn from the compositional variation of minerals.

Crystallization and preservation of garnet in high-Mg# adakitic porphyries during post-collisional extension

The ~233 Ma (Dan *et al.*, 2018a) peak-metamorphism age of the eclogites exposed 60 km southwest of the Baohu diorites (Fig. 1a) marks the collision between the Northern and Southern Qiangtang terranes. The Late Triassic (225–205 Ma) magmatic rocks form a linear belt parallel to the Longmu Co–Shuanghu suture (Fig. 1a), and this magmatic flare-up is contemporaneous with the exhumation of the eclogites, implying that the central Qiangtang area was undergoing post-collisional extension induced by the breakoff of the subducted Paleo-Tethyan oceanic slab in the Late Triassic (e.g. Wu *et al.*, 2016). The identification of Late Triassic oceanic island basalt (OIB)–type basalts around the Longmu Co–Shuanghu suture also suggested that the shallow breakoff triggered decompression melting of upwelling asthenosphere above the detached slab (Zhang *et al.*, 2011). The upwelling of asthenosphere upon breakoff can cause a thermal perturbation and shallow melting of the overriding metasomatized lithospheric mantle (Davies & von Blanckenburg, 1995).

Although the water-rich Type 1 diorites have major element compositions (e.g. Mg#) similar to primitive arc andesites (Kelemen *et al.*, 2003), they are distinguished from the latter by more enriched Nd and Sr isotopic compositions. This can be explained by derivation of primary magmas from an enriched mantle source, or by later assimilation of enriched crustal material. The magma differentiation here is operated by fractional crystallization and assimilation of isotopically depleted,

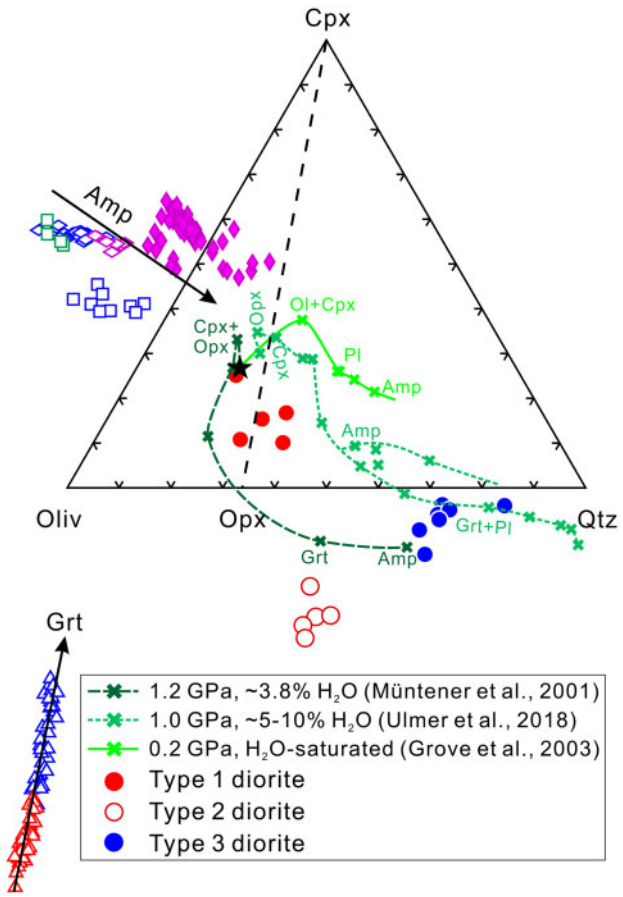

Fig. 13. Pseudo-ternary olivine–clinopyroxene–quartz (Ol–Cpx–Qtz) diagram projected from plagioclase. The compositions of the Baohu diorites, amphibole and garnet have been recalculated into mineral end member components after the method of Grove (1993). Liquid lines of descent produced by crystallization of a primitive basaltic andesite (black star) at pressures of 1·2, 1·0 and 0·2 GPa are shown for comparison (Müntener *et al.*, 2001; Grove *et al.*, 2003; Ulmer *et al.*, 2018). The 1·0 GPa experimental liquid lines of descent diverge into two branches that represent the clinopyroxene– and orthopyroxene–amphibole peritectic boundaries. Note that the phase boundaries that vary with pressure are not well constrained and are not shown. The mineral names next to liquid lines of descent indicate their first appearance. Arrows in mineral compositional fields indicate evolution with decreasing temperature. Other symbols are as in Fig. 3, 9 and 11. Opx, orthopyroxene; Cpx, clinopyroxene; Pl, plagioclase; Amp, amphibole; Grt, garnet.

juvenile crustal material. Thus, the Type 1 diorites may originate from a metasomatized lithospheric mantle which had been isotopically enriched by subducted sediments, continental material and eroded forearc crust (e.g. Goss *et al.*, 2013; Couzinié *et al.*, 2016) during oceanic and continental subduction shortly preceding slab breakoff. Post-collisional magmas derived from lithospheric mantle metasomatized by subducted continental material are usually characterized by more enriched isotopic composition compared with classical arc magmas (related to oceanic subduction; Couzinié *et al.*, 2016). Alternatively, the enriched Sr–Nd isotopic compositions of metasomatized ancient lithospheric mantle may reflect the time-integrated effect of enrichment in the LREEs and Rb relative to Sr. Considering the Mesozoic tectonic evolution of the Northern Qiangtang terrane, we suggest that the water-rich Type 1 diorites were most likely generated by shallow melting of subduction-enriched lithospheric mantle during oceanic slab breakoff.

The magma ascent *P–T* path in the phase-equilibrium diagram (Fig. 12b) can explain why most of volcanic rocks or porphyries lack garnet phenocrysts even if their mantle-derived parent magmas underwent crystallization at the base of the crust. Mantle-derived metaluminous magmas do not have garnet as a liquidus phase until their derivative liquids become slightly peraluminous due to the early fractionation of pyroxene and amphibole (Fig. 12b, 13). The crystallization of garnet requires that mantle-derived magmas stall, cool isobarically and differentiate at the base of the crust (dashed blue line in Fig. 12b); but decompression cooling may cause magmas to move away from the stability field of garnet (dashed red line in Fig. 12b). Finally, the preservation of garnet in volcanic rocks or porphyries requires the rapid ascent of host magmas after garnet crystallization in the lower crust, because garnet may be resorbed at low pressure or settle out of the magma due to its high density. The presence of deep-seated faults can promote rapid ascent of garnet-bearing magmas. In addition, crystallization of Ca-rich almandine is favored from water-rich parent magmas (Green, 1992; Alonso-Perez *et al.*, 2009), such as the Baohu diorites with >5 wt % H_2O. High volatile contents might have also enhanced the rapid ascent of the magmas. These circumstances could be attained in areas that undergo lithospheric extension following or concurrent with subduction (e.g. Fitton, 1972; Harangi *et al.*, 2001; Bach *et al.*, 2012; Luo *et al.*, 2018). For example, the thick lithosphere formed during the initial stages of continental collision following oceanic subduction would undergo the large-scale extension due to oceanic slab breakoff or the subsequent orogenic collapse (Harangi *et al.*, 2001; Luo *et al.*, 2018). In the study area, the rapid exhumation of high-density eclogites (Fig. 1a; Zhai *et al.*, 2011) indicates the presence of lithosphere-scale faults around the Longmu Co–Shuanghu suture in the Late Triassic, which probably prevented some of the early-crystallized garnet in Type 2 and 3 diorite porphyries from being resorbed into the melt. In conclusion, the crystallization and preservation of garnet in volcanic rocks and porphyries requires that the water-rich magma be stored temporarily in the lower crustal magma chambers to precipitate garnet, and then brought rapidly to the surface in an extensional setting.

Generation of high-Mg# adakitic rocks without interaction between crust-derived melt and the mantle

Modern arc adakites with higher MgO contents and Mg# values than the products of high-pressure metabasalt melting experiments have been attributed to the

interaction between melts derived from subducted oceanic crust and/or eroded forearc crust and peridotite in the mantle wedge (Fig. 3; Kay, 1978; Kay et al., 1993, 2019; Yogodzinski *et al.*, 1995; Rapp *et al.*, 1999; Goss *et al.*, 2013); and continental high-Mg# adakitic rocks in non-arc environments were thought to have been generated by interaction between melts derived from delaminated lower continental crust and overlying mantle peridotites (Gao *et al.*, 2004; Wang *et al.*, 2006). In addition, some intermediate to felsic veins and glassy inclusions in mantle peridotite xenoliths in arc lavas have high Mg# values and Sr/Y ratios, similar to those of adakites erupted at the surface (Schiano *et al.*, 1995; Kepezhinskas *et al.*, 1996). These metasomatized peridotite xenoliths from the sub-arc mantle provide direct evidence for interaction between crust-derived adakitic melts and mantle peridotite.

Whether high-Mg# adakitic rocks can be regarded as a direct indicator of interaction between crust-derived melt and mantle remains debated. High-Mg# andesites can form by the fractional crystallization of a primitive basalt at high oxygen or water fugacity (fO_2 or fH_2O), driving early crystallization of abundant Fe–Ti oxides, almandine garnet, and amphibole (e.g. Sisson & Grove, 1993); as Fe–Ti oxides and almandine garnet have higher Fe–Mg solid–liquid partition coefficients than olivine and pyroxene (Green, 1977; Alonso-Perez *et al.*, 2009; Ulmer *et al.*, 2018), and their fractionation can suppress the reduction in Mg# values of residual liquids (e.g. Zellmer *et al.*, 2012). Fractional crystallization of a primitive andesite (Mg# $>$ 60) can also generate high-Mg# andesites under a wide range of conditions (Fig. 3; Müntener *et al.*, 2001; Grove *et al.*, 2003; Kelemen *et al.*, 2003; Wang *et al.*, 2018a), and high-Mg# andesites derived from primitive andesites or from basalts by garnet ($\pm$ amphibole) fractionation will also have adakitic geochemical characteristics. Although garnet-bearing rocks have been found in tectonically exposed arc crustal sections (Jagoutz, 2010) and in basalt-hosted xenoliths (Lee *et al.*, 2006), it is challenging to distinguish between restite (metamorphic product) and cumulate origins of these rocks and to directly associate them with high-Mg# adakitic rocks. The Baohu diorite porphyries in central Tibet are a rare example of garnet-bearing high-Mg# adakitic rocks formed by the fractionation of pyroxene, amphibole, and garnet from a primitive andesitic parent, rather than by interaction between crust-derived melt and the mantle. Recent studies also suggested that the garnet fractionation of arc magma can explain the preferential association of porphyry copper systems with calc-alkaline magmas and thicker arcs (Tang *et al.*, 2018; Lee and Tang, 2020).

Thus, high-Mg# adakitic rocks are not indicative of interaction between crust-derived melt and the mantle, although this interaction is potentially a frequent occurrence in the mantle wedge. It may be difficult to distinguish melt–mantle interaction from intra-crustal magma differentiation solely using the whole-rock geochemistry of high-Mg# adakitic rocks, especially when late-stage magma differentiation (e.g. assimilation and fractional crystallization) obscures primary melt features. In this study, we found non-adakitic diorite porphyries with Mg# values $>$ 62, which represent the parental magmas of high-Mg# adakitic rocks. The compositional variations of the early-crystallized garnet and amphibole provide direct mineralogical evidence for lower-crustal (~1 GPa) garnet fractionation, which ultimately led to the generation of high-Mg# adakitic rocks.

CONCLUSIONS

We identified Late Triassic (~220 Ma) garnet-bearing high-Mg# (Mg# = 45–56) adakitic diorite porphyries and garnet-free non-adakitic diorite porphyries with Mg# values $>$ 62 in central Tibet. Consistent compositional correlation between Ca-rich garnet crystals, their host rocks, and zircon autocrysts suggests that the garnet crystals grew in their host magmas. Variations in whole-rock and mineral compositions show that the high-Mg# adakitic rocks were most likely produced by the fractionation of pyroxene, amphibole, and garnet from garnet-free non-adakitic diorite porphyries. The crystallization of garnet was driven by isobaric (~1 GPa) cooling of hydrous (H_2O $>$5 wt %) parent magmas at the base of the crust. This study provides direct mineralogical evidence of the importance of lower-crustal garnet fractionation in the generation of high-Mg# adakitic rocks, and shows that the relationship between high-Mg# adakitic rocks and interaction between crust-derived melt and mantle is not necessarily causal, although this interaction is potentially a frequent occurrence in the mantle wedge.

ACKNOWLEDGEMENTS

This manuscript was greatly improved by constructive reviews by Professors Suzanne Kay, Tomoyuki Shibata, Cin-Ty Lee, and Marlina Elburg, as well as discussion with Dr Xiu-Zheng Zhang. We thank Professors Georg Zellmer and Marjorie Wilson for editorial handling. We appreciate Dan Wu, Peng-Li He, and Le Zhang for help with the LA-ICPMS and EPMA analyses.

FUNDING

This study was supported by the National Natural Science Foundation of China (41630208, 91855215 and 42021002), the Strategic Priority Research Program (A) of the Chinese Academy of Sciences (grant no. XDA2007030402), the Second Tibetan Plateau Scientific Expedition and Research (STEP) (2019QZKK0702), the National Key R & D Program of China (2016YFC0600407), the Key Program of the Chinese Academy of Sciences (QYZDJ-SSW-DQC026) and Chinese Academy of Science (GIGCAS 135 project 135TP201601). This is contribution No. IS-3000 from GIGCAS.

REFERENCES

Alonso-Perez, R., Müntener, O. & Ulmer, P. (2009). Igneous garnet and amphibole fractionation in the roots of island arcs: experimental constraints on andesitic liquids. *Contributions to Mineralogy and Petrology* **157**, 541–558.

Atherton, M. P. & Petford, N. (1993). Generation of Sodium-Rich Magmas from Newly Underplated Basaltic Crust. *Nature* **362**, 144–146.

Bach, P., Smith, I. E. M. & Malpas, J. G. (2012). The Origin of Garnets in Andesitic Rocks from the Northland Arc, New Zealand, and their Implication for Sub-arc Processes. *Journal of Petrology* **53**, 1169–1195.

Bachmann, O. & Dungan, M. A. (2002). Temperature-induced Al-zoning in hornblendes of the Fish Canyon magma, Colourado. *American Mineralogist* **87**, 1062–1076.

Cabero, M. T., Mecoleta, S. & Lopez-Moro, F. J. (2012). OPTIMASBA: A Microsoft Excel workbook to optimise the mass-balance modelling applied to magmatic differentiation processes and subsolidus overprints. *Computers & Geosciences* **42**, 206–211.

Castillo, P. R., Janney, P. E. & Solidum, R. U. (1999). Petrology and geochemistry of Camiguin Island, southern Philippines: insights to the source of adakites and other lavas in a complex arc setting. *Contributions to Mineralogy and Petrology* **134**, 33–51.

Corfu, F., Hanchar, J. M., Hoskin, P. W. O. & Kinny, P. (2003). Atlas of Zircon Textures. *Reviews in Mineralogy and Geochemistry* **53**, 469–500.

Couzinié, S., Laurent, O., Moyen, J. F., Zeh, A., Bouilhol, P. & Villaros, A. (2016). Post-collisional magmatism: Crustal growth not identified by zircon Hf-O isotopes. *Earth and Planetary Science Letters* **456**, 182–195.

Dan, W., Wang, Q., Li, X. H., Tang, G. J., Zhang, C. F., Zhang, X. Z. & Wang, J. (2019). Low delta O-18 magmas in the carboniferous intra-oceanic arc, central Tibet: Implications for felsic magma generation and oceanic arc accretion. *Lithos* **326**, 28–38.

Dan, W., Wang, Q., White, W. M., Zhang, X.-Z., Tang, G.-J., Jiang, Z.-Q., Hao, L.-L. & Ou, Q. (2018a). Rapid formation of eclogites during a nearly closed ocean: Revisiting the Pianshishan eclogite in Qiangtang, central Tibetan Plateau. *Chemical Geology* **477**, 112–122.

Dan, W., Wang, Q., Zhang, X.-Z., Zhang, C., Tang, G.-J., Wang, J., Ou, Q., Hao, L.-L. & Qi, Y. (2018b). Magmatic record of Late Devonian arc-continent collision in the northern Qiangtang, Tibet: Implications for the early evolution of East Paleo-Tethys Ocean. *Lithos* **308-309**, 104–117.

Davidson, J., Morgan, D., Charlier, B., Harlou, R. & Hora, J. (2007). Microsampling and isotopic analysis of igneous rocks: implications for the study of magmatic systems. *Annual Review of Earth and Planetary Sciences* **35**, 273–311.

Davies, J. H. & Von Blanckenburg, F. (1995). Slab Breakoff - a Model of Lithosphere Detachment and Its Test in the Magmatism and Deformation of Collisional Orogens. *Earth and Planetary Science Letters* **129**, 85–102.

Day, R. A., Green, T. H. & Smith, I. E. M. (1992). The Origin and Significance of Garnet Phenocrysts and Garnet-Bearing Xenoliths in Miocene Calc-Alkaline Volcanics from Northland, New-Zealand. *Journal of Petrology* **33**, 125–161.

Defant, M. J. & Drummond, M. S. (1990). Derivation of some modern arc magmas by melting of young subducted lithosphere. *Nature* **347**, 662–665.

Erdmann, S., Martel, C., Pichavant, M. & Kushnir, A. (2014). Amphibole as an archivist of magmatic crystallization conditions: problems, potential, and implications for inferring magma storage prior to the paroxysmal 2010 eruption of Mount Merapi, Indonesia. *Contributions to Mineralogy and Petrology* **167**.

Fitton, J. G. (1972). The genetic significance of almandine-pyrope phenocrysts in the calc-alkaline Borrowdale Volcanic Group, Northern England. *Contributions to Mineralogy and Petrology* **36**, 231–248.

Gao, S., Rudnick, R. L., Yuan, H. L., Liu, X. M., Liu, Y. S., Xu, W. L., Ling, W. L., Ayers, J., Wang, X. C. & Wang, Q. H. (2004). Recycling lower continental crust in the North China craton. *Nature* **432**, 892–897.

Goss, A. R., Kay, S. M. & Mpodozis, C. (2013). Andean Adakite-like high-Mg Andesites on the Northern Margin of the Chilean-Pampean Flat-slab (27-28.5°S) Associated with Frontal Arc Migration and Fore-arc Subduction Erosion. *Journal of Petrology* **54**, 2193–2234.

Green, T. H. (1977). Garnet in Silicic Liquids and Its Possible Use as a *P–T* Indicator. *Contributions to Mineralogy and Petrology* **65**, 59–67.

Green, T. H. (1982). 'Anatexis of Mafic Crust and High Pressure Crystallization of Andesite', In: Thorpe, R. S. (ed.) *Andesites: Orogenic Andesites and Related Rocks*. Chichester: John Wiley, 465–487.

Green, T. H. (1992). Experimental Phase-Equilibrium Studies of Garnet-Bearing I-Type Volcanics and High-Level Intrusives from Northland, New-Zealand. *Earth and Environmental Science Transactions of the Royal Society of Edinburgh* **83**, 429–438.

Green, T. H. & Ringwood, A. E. (1968). Origin of garnet phenocrysts in calc-alkaline rocks. *Contributions to Mineralogy and Petrology* **18**, 163–174.

Grove, T. L. (1993). Corrections to expressions for calculating mineral components in "Origin of calc-alkaline series lavas at medicine lake volcano by fractionation, assimilation and mixing" and "Experimental petrology of normal MORB near the kane fracture zone: 22°-25°N, mid-atlantic ridge. *Contributions to Mineralogy and Petrology* **114**, 422–424.

Grove, T. L., Elkins-Tanton, L. T., Parman, S. W., Chatterjee, N., Müntener, O. & Gaetani, G. A. (2003). Fractional crystallization and mantle-melting controls on calc-alkaline differentiation trends. *Contributions to Mineralogy and Petrology* **145**, 515–533.

Harangi, S., Downes, H., Kosa, L., Szabo, C., Thirlwall, M. F., Mason, P. R. D. & Mattey, D. (2001). Almandine garnet in calc-alkaline volcanic rocks of the northern Pannonian Basin (eastern-central Europe): Geochemistry, petrogenesis and geodynamic implications. *Journal of Petrology* **42**, 1813–1843.

Hildreth, W. & Moorbath, S. (1988). Crustal contributions to arc magmatism in the Andes of central Chile. *Contributions to Mineralogy and Petrology* **98**, 455–489.

Huang, X.-L., Xu, Y.-G., Lo, C.-H., Wang, R.-C. & Lin, C.-Y. (2007). Exsolution lamellae in a clinopyroxene megacryst aggregate from Cenozoic basalt, Leizhou Peninsula, South China: petrography and chemical evolution. *Contributions to Mineralogy and Petrology* **154**, 691–705.

Humphreys, M. C. S., Cooper, G. F., Zhang, J., Loewen, M., Kent, A. J. R., Macpherson, C. G. & Davidson, J. P. (2019). Unravelling the complexity of magma plumbing at Mount St. Helens: a new trace element partitioning scheme for amphibole. *Contributions to Mineralogy and Petrology* **174**, 1–15.

Jagoutz, O. E. (2010). Construction of the granitoid crust of an island arc. Part II: a quantitative petrogenetic model. *Contributions to Mineralogy and Petrology* **160**, 359–381.

Kay, R. W. (1978). Aleutian magnesian andesites: melts from subducted Pacific ocean crust. *Journal of Volcanology and Geothermal Research* **4**, 117–132.

Kay, S. M., Jicha, B. R., Citron, G. L., Kay, R. W., Tibbetts, A. K. & Rivera, T. A. (2019). The Calc-Alkaline Hidden Bay and Kagalaska Plutons and the Construction of the Central Aleutian Oceanic Arc Crust. *Journal of Petrology* **60**, 393–439.

Kay, S. M., Ramos, V. A. & Marquez, M. (1993). Evidence in Cerro-Pampa Volcanic-Rocks for Slab-Melting Prior to Ridge-Trench Collision in Southern South-America. *The Journal of Geology* **101**, 703–714.

Kelemen, P. B. (1995). Genesis of high Mg# andesites and the continental crust. *Contributions to Mineralogy and Petrology* **120**, 1–19.

Kelemen, P. B., Yogodzinski, G. M. & Scholl, D. W. (2003). Along-Strike Variation in the Aleutian Island Arc: Genesis of High Mg# Andesite and Implications for Continental Crust. *Inside the Subduction Factory: American Geophysical Union* 223–276.

Kepezhinskas, P., Defant, M. J. & Drummond, M. S. (1996). Progressive enrichment of island arc mantle by melt-peridotite interaction inferred from Kamchatka xenoliths. *Geochimica Et Cosmochimica Acta* **60**, 1217–1229.

Kiss, B., Harangi, S., Ntaflos, T., Mason, P. R. D. & Pál-Molnár, E. (2014). Amphibole perspective to unravel pre-eruptive processes and conditions in volcanic plumbing systems beneath intermediate arc volcanoes: a case study from Ciomadul volcano (SE Carpathians). *Contributions to Mineralogy and Petrology* **167**.

Krawczynski, M. J., Grove, T. L. & Behrens, H. (2012). Amphibole stability in primitive arc magmas: effects of temperature, H2O content, and oxygen fugacity. *Contributions to Mineralogy and Petrology* **164**, 317–339.

Lanzirotti, A. (1995). Yttrium Zoning in Metamorphic Garnets. *Geochimica Et Cosmochimica Acta* **59**, 4105–4110.

Lee, C. T. A., Cheng, X. & Horodyskyj, U. (2006). The development and refinement of continental arcs by primary basaltic magmatism, garnet pyroxenite accumulation, basaltic recharge and delamination: insights from the Sierra Nevada, California. *Contributions to Mineralogy and Petrology* **151**, 222–242.

Lee, C. T. A. & Tang, M. (2020). How to make porphyry copper deposits. *Earth and Planetary Science Letters* **529**, 115868.

Li, X. H., Li, Z. X., Wingate, M. T. D., Chung, S. L., Liu, Y., Lin, G. C. & Li, W. X. (2006). Geochemistry of the 755 Ma Mundine Well dyke swarm, northwestern Australia: Part of a Neoproterozoic mantle superplume beneath Rodinia? *Precambrian Research* **146**, 1–15.

Li, X. H., Long, W. G., Li, Q. L., Liu, Y., Zheng, Y. F., Yang, Y. H., Chamberlain, K. R., Wan, D. F., Guo, C. H., Wang, X. C. & Tao, H. (2010). Penglai Zircon Megacrysts: A Potential New Working Reference Material for Microbeam Determination of Hf-O Isotopes and U-Pb Age. *Geostandards and Geoanalytical Research* **34**, 117–134.

Li, X. H., Tang, G. Q., Gong, B., Yang, Y. H., Hou, K. J., Hu, Z. C., Li, Q. L., Liu, Y. & Li, W. X. (2013). Qinghu zircon: A working reference for microbeam analysis of U-Pb age and Hf and O isotopes. *Chinese Science Bulletin* **58**, 4647–4654.

Liu, Y., Gao, S., Hu, Z., Gao, C., Zong, K. & Wang, D. (2010). Continental and oceanic crust recycling-induced melt–peridotite interactions in the Trans-North China Orogen: U–Pb dating, Hf isotopes and trace elements in zircons from mantle xenoliths. *Journal of Petrology* **51**, 537–571.

Locock, A. J. (2014). An Excel spreadsheet to classify chemical analyses of amphiboles following the IMA 2012 recommendations. *Computers & Geosciences* **62**, 1–11.

Ludwig, K. R. (2003). User's manual for Isoplot 3.00: a geochronological toolkit for Microsoft Excel: Kenneth R. Ludwig.

Luo, B. J., Zhang, H. F., Xu, W. C., Yang, H., Zhao, J. H., Guo, L., Zhang, L. Q., Tao, L., Pan, F. B. & Gao, Z. (2018). The Magmatic Plumbing System for Mesozoic High-Mg Andesites, Garnet-bearing Dacites and Porphyries, Rhyolites and Leucogranites from West Qinling, Central China. *Journal of Petrology* **59**, 447–481.

Macpherson, C. G., Dreher, S. T. & Thirlwall, M. F. (2006). Adakites without slab melting: high pressure differentiation of island arc magma, Mindanao, the Philippines. *Earth and Planetary Science Letters* **243**, 581–593.

Martin, H., Smithies, R. H., Rapp, R., Moyen, J. F. & Champion, D. (2005). An overview of adakite, tonalite-trondhjemite-granodiorite (TTG), and sanukitoid: relationships and some implications for crustal evolution. *Lithos* **79**, 1–24.

Mitchell, A. L. & Grove, T. L. (2015). Melting the hydrous, subarc mantle: the origin of primitive andesites. *Contributions to Mineralogy and Petrology* **170**.

Muhling, J. R. & Griffin, B. J. (1991). On Recasting Garnet Analyses into End-Member Molecules - Revisited. *Computers & Geosciences* **17**, 161–170.

Mungall, J. E. (2002). Roasting the mantle: Slab melting and the genesis of major Au and Au-rich Cu deposits. *Geology* **30**, 915–918.

Müntener, O., Kelemen, P. B. & Grove, T. L. (2001). The role of H2O during crystallization of primitive arc magmas under uppermost mantle conditions and genesis of igneous pyroxenites: an experimental study. *Contributions to Mineralogy and Petrology* **141**, 643–658.

Nesbitt, H. W. & Young, G. M. (1982). Early Proterozoic Climates and Plate Motions Inferred from Major Element Chemistry of Lutites. *Nature* **299**, 715–717.

Prouteau, G. & Scaillet, B. (2003). Experimental constraints on the origin of the 1991 Pinatubo dacite. *Journal of Petrology* **44**, 2203–2241.

Pullen, A., Kapp, P., Gehrels, G. E., Vervoort, J. D. & Ding, L. (2008). Triassic continental subduction in central Tibet and Mediterranean-style closure of the Paleo-Tethys Ocean. *Geology* **36**, 351–354.

Putirka, K. (2016). Amphibole thermometers and barometers for igneous systems and some implications for eruption mechanisms of felsic magmas at arc volcanoes. *American Mineralogist* **101**, 841–858.

Rapp, R. P., Norman, M. D., Laporte, D., Yaxley, G. M., Martin, H. & Foley, S. F. (2010). Continent Formation in the Archean and Chemical Evolution of the Cratonic Lithosphere: Melt-Rock Reaction Experiments at 3-4 GPa and Petrogenesis of Archean Mg-Diorites (Sanukitoids). *Journal of Petrology* **51**, 1237–1266.

Rapp, R. P., Shimizu, N., Norman, M. D. & Applegate, G. S. (1999). Reaction between slab-derived melts and peridotite in the mantle wedge: experimental constraints at 3.8 GPa. *Chemical Geology* **160**, 335–356.

Rapp, R. P. & Watson, E. B. (1995). Dehydration melting of metabasalt at 8–32 kbar: implications for continental growth and crust-mantle recycling. *Journal of Petrology* **36**, 891–931.

Ribeiro, J. M., Maury, R. C. & Gregoire, M. (2016). Are Adakites Slab Melts or High-pressure Fractionated Mantle Melts? *Journal of Petrology* **57**, 839–862.

Ridolfi, F. & Renzulli, A. (2012). Calcic amphiboles in calc-alkaline and alkaline magmas: thermobarometric and chemometric empirical equations valid up to 1,130°C and 2.2 GPa. *Contributions to Mineralogy and Petrology* **163**, 877–895.

Ridolfi, F., Renzulli, A. & Puerini, M. (2010). Stability and chemical equilibrium of amphibole in calc-alkaline magmas: an

overview, new thermobarometric formulations and application to subduction-related volcanoes. *Contributions to Mineralogy and Petrology* **160**, 45–66.

Rubatto, D. & Hermann, J. (2007). Experimental zircon/melt and zircon/garnet trace element partitioning and implications for the geochronology of crustal rocks. *Chemical Geology* **241**, 38–61.

Scaillet, B. & Evans, B. W. (1999). The 15 June 1991 eruption of Mount Pinatubo. I. Phase equilibria and pre-eruption P-T-fO2-fH2O conditions of the dacite magma. *Journal of Petrology* **40**, 381–411.

Schiano, P., Clocchiatti, R., Shimizu, N., Maury, R. C., Jochum, K. P. & Hofmann, A. W. (1995). Hydrous, Silica-Rich Melts in the Sub-Arc Mantle and Their Relationship with Erupted Arc Lavas. *Nature* **377**, 595–600.

Sen, C. & Dunn, T. (1994). Dehydration Melting of a Basaltic Composition Amphibolite at 1.5 and 2.0 GPa: Implications for the Origin of Adakites. *Contributions to Mineralogy and Petrology* **117**, 394–409.

Shibata, T., Yoshimoto, M., Fujii, T. & Nakada, S. (2015). Geochemical and Sr-Nd isotopic characteristics of Quaternary Magmas from the Pre-Komitake volcano. *Journal of Mineralogical and Petrological Sciences* **110**, 65–70.

Shuto, K., Sato, M., Kawabata, H., Osanai, Y., Nakano, N. & Yashima, R. (2013). Petrogenesis of Middle Miocene Primitive Basalt, Andesite and Garnet-bearing Adakitic Rhyodacite from the Ryozen Formation: Implications for the Tectono-magmatic Evolution of the NE Japan Arc. *Journal of Petrology* **54**, 2413–2454.

Sisson, T. W. & Grove, T. L. (1993). Experimental investigations of the role of H2O in calc-alkaline differentiation and subduction zone magmatism. *Contributions to Mineralogy and Petrology* **113**, 143–166.

Sisson, T. W. & Kelemen, P. B. (2018). Near-solidus melts of MORB+4 wt% H2O at 0.8-2.8 GPa applied to issues of subduction magmatism and continent formation. *Contributions to Mineralogy and Petrology* **173**, 70.

Sláma, J., Kosler, J., Condon, D. J., Crowley, J. L., Gerdes, A., Hanchar, J. M., Horstwood, M. S. A., Morris, G. A., Nasdala, L., Norberg, N., Schaltegger, U., Schoene, B., Tubrett, M. N. & Whitehouse, M. J. (2008). Plesovice zircon - A new natural reference material for U-Pb and Hf isotopic microanalysis. *Chemical Geology* **249**, 1–35.

Streck, M. J., Leeman, W. P. & Chesley, J. (2007). High-magnesian andesite from Mount Shasta: A product of magma mixing and contamination, not a primitive mantle melt. *Geology* **35**, 351–354.

Sun, S.-S. & McDonough, W. F. (1989). Chemical and isotopic systematics of oceanic basalts: implications for mantle composition and processes. *Geological Society, London, Special Publications* **42**, 313–345.

Tang, G. J., Wang, Q., Wyman, D. A., Chung, S. L., Chen, H. Y. & Zhao, Z. H. (2017). Genesis of pristine adakitic magmas by lower crustal melting: A perspective from amphibole composition. *Journal of Geophysical Research-Solid Earth* **122**, 1934–1948.

Tang, M., Erdman, M., Eldridge, G. & Lee, C. T. A. (2018). The redox "filter" beneath magmatic orogens and the formation of continental crust. *Science Advances* **4**, eaar4444.

Tatsumi, Y., Suzuki, T., Kawabata, H., Sato, K., Miyazaki, T., Chang, Q., Takahashi, T., Tani, K., Shibata, T. & Yoshikawa, M. (2006). The petrology and geochemistry of Oto-Zan composite lava flow on Shodo-Shima Island, SW Japan: Remelting of a solidified high-mg andesite magma. *Journal of Petrology* **47**, 595–629.

Tiepolo, M., Oberti, R., Zanetti, A., Vannucci, R. & Foley, S. F. (2007). Trace-element partitioning between amphibole and silicate melt. *Reviews in Mineralogy and Geochemistry* **67**, 417–452.

Tu, X., Zhang, H., Deng, W., Ling, M., Liang, H., Liu, Y. & Sun, W. (2011). Application of RESOlution in-situ laser ablation ICP-MS in trace element analyses. *Geochimica* **40**, 83–98.

Ulmer, P., Kaegi, R. & Müntener, O. (2018). Experimentally Derived Intermediate to Silica-rich Arc Magmas by Fractional and Equilibrium Crystallization at 1.0 GPa: an Evaluation of Phase Relationships, Compositions, Liquid Lines of Descent and Oxygen Fugacity. *Journal of Petrology* **59**, 11–58.

Van Orman, J. A., Grove, T. L., Shimizu, N. & Layne, G. D. (2002). Rare earth element diffusion in a natural pyrope single crystal at 2.8 GPa. *Contributions to Mineralogy and Petrology* **142**, 416–424.

Wang, J., Gou, G.-N., Wang, Q., Zhang, C., Dan, W., Wyman, D. A. & Zhang, X.-Z. (2018a). Petrogenesis of the Late Triassic diorites in the Hoh Xil area, northern Tibet: Insights into the origin of the high-Mg# andesitic signature of continental crust. *Lithos* **300-301**, 348–360.

Wang, J., Wang, Q., Zhang, C., Dan, W., Qi, Y., Zhang, X.-Z. & Xia, X.-P. (2018b). Late Permian Bimodal Volcanic Rocks in the Northern Qiangtang Terrane, Central Tibet: Evidence for Interaction Between the Emeishan Plume and the Paleo-Tethyan Subduction System. *Journal of Geophysical Research: Solid Earth* **123**, 6540–6561.

Wang, Q., McDermott, F., Xu, J. F., Bellon, H. & Zhu, Y. T. (2005). Cenozoic K-rich adakitic volcanic rocks in the Hohxil area, northern Tibet: Lower-crustal melting in an intracontinental setting. *Geology* **33**, 465–468.

Wang, Q., Xu, J. F., Jian, P., Bao, Z. W., Zhao, Z. H., Li, C. F., Xiong, X. L. & Ma, J. L. (2006). Petrogenesis of adakitic porphyries in an extensional tectonic setting, dexing, South China: Implications for the genesis of porphyry copper mineralization. *Journal of Petrology* **47**, 119–144.

Waters, L. E. & Lange, R. A. (2015). An updated calibration of the plagioclase-liquid hygrometer-thermometer applicable to basalts through rhyolites. *American Mineralogist* **100**, 2172–2184.

Weis, D., Kieffer, B., Maerschalk, C., Pretorius, W. & Barling, J. (2005). High-precision Pb-Sr-Nd-Hf isotopic characterization of USGS BHVO-1 and BHVO-2 reference materials. *Geochemistry Geophysics Geosystems* **6**, Q02002.

Wood, B. J. & Turner, S. P. (2009). Origin of primitive high-Mg andesite: Constraints from natural examples and experiments. *Earth and Planetary Science Letters* **283**, 59–66.

Wu, H., Li, C., Chen, J. & Xie, C. (2016). Late Triassic tectonic framework and evolution of Central Qiangtang, Tibet, SW China. *Lithosphere* **8**, 141–149.

Xie, L., Zhang, Y., Zhang, H., Sun, J. & Wu, F. (2008). In situ simultaneous determination of trace elements, U-Pb and Lu-Hf isotopes in zircon and baddeleyite. *Chinese Science Bulletin* **53**, 1565–1573.

Yin, A. & Harrison, T. M. (2000). Geologic Evolution of the Himalayan-Tibetan Orogen. *Annual Review of Earth and Planetary Sciences* **28**, 211–280.

Yogodzinski, G. M., Kay, R. W., Volynets, O. N., Koloskov, A. V. & Kay, S. M. (1995). Magnesian andesite in the western Aleutian Komandorsky region: Implications for slab melting and processes in the mantle wedge. *Geological Society of America Bulletin* **107**, 505–519.

Yuan, C., Sun, M., Xiao, W. J., Wilde, S., Li, X. H., Liu, X. H., Long, X. P., Xia, X. P., Ye, K. & Li, J. L. (2009). Garnet-bearing tonalitic porphyry from East Kunlun, Northeast Tibetan Plateau: implications for adakite and magmas from the MASH Zone. *International Journal of Earth Sciences* **98**, 1489–1510.

Zellmer, G. F., Iizuka, Y., Miyoshi, M., Tamura, Y. & Tatsumi, Y. (2012). Lower crustal H2O controls on the formation of adakitic melts. *Geology* **40**, 487–490.

Zhai, Q.-G., Jahn, B.-M., Su, L., Wang, J., Mo, X.-X., Lee, H.-Y., Wang, K-L. & Tang, S. (2013). Triassic arc magmatism in the Qiangtang area, northern Tibet: Zircon U–Pb ages, geochemical and Sr–Nd–Hf isotopic characteristics, and tectonic implications. *Journal of Asian Earth Sciences* **63**, 162–178.

Zhai, Q. G., Zhang, R. Y., Jahn, B. M., Li, C., Song, S. G. & Wang, J. (2011). Triassic eclogites from central Qiangtang, northern Tibet, China: petrology, geochronology and metamorphic P–T path. *Lithos* **125**, 173–189.

Zhang, K.-J., Cai, J.-X., Zhang, Y.-X. & Zhao, T.-P. (2006). Eclogites from central Qiangtang, northern Tibet (China) and tectonic implications. *Earth and Planetary Science Letters* **245**, 722–729.

Zhang, K.-J., Tang, X.-C., Wang, Y. & Zhang, Y.-X. (2011). Geochronology, geochemistry, and Nd isotopes of early Mesozoic bimodal volcanism in northern Tibet, western China: Constraints on the exhumation of the central Qiangtang metamorphic belt. *Lithos* **121**, 167–175.

Zhang, L., Ren, Z. Y., Xia, X. P., Li, J. & Zhang, Z. F. (2015). IsotopeMaker: A Matlab program for isotopic data reduction. *International Journal of Mass Spectrometry* **392**, 118–124.

Zhang, X. Z., Dong, Y. S., Wang, Q., Dan, W., Zhang, C., Deng, M. R., Xu, W., Xia, X. P., Zeng, J. P. & Liang, H. (2016). Carboniferous and Permian evolutionary records for the Paleo-Tethys Ocean constrained by newly discovered Xiangtaohu ophiolites from central Qiangtang, central Tibet. *Tectonics* **35**, 1670–1686.

Zhou, J. S., Yang, Z. S., Hou, Z. Q. & Wang, Q. (2020). Amphibole-rich cumulate xenoliths in the Zhazhalong intrusive suite, Gangdese arc: Implications for the role of amphibole fractionation during magma evolution. *American Mineralogist* **105**, 262–275.